

Variational Textured Dirichlet Process Mixture Model with Pairwise Constraint for Unsupervised Classification of Polarimetric SAR Images

Chi Liu, Heng-Chao Li, *Senior Member, IEEE*, Wenzhi Liao, *Senior Member, IEEE*, Wilfried Philips, *Senior Member, IEEE*, and William J. Emery, *Fellow, IEEE*

Abstract—This paper proposes an unsupervised classification method for multilook polarimetric synthetic aperture radar (PolSAR) data. The proposed method simultaneously deals with the heterogeneity and incorporates the local correlation in PolSAR images. Specifically, within the probabilistic framework of the Dirichlet process mixture model (DPMM), an observed PolSAR data point is described by the multiplication of a Wishart-distributed component and a class-dependent random variable (i.e., the textual variable). This modeling scheme leads to the proposed textured DPMM (tDPMM), which possesses more flexibility in characterizing PolSAR data in heterogeneous areas and from high-resolution images due to the introduction of the class-dependent texture variable. The proposed tDPMM is learned by solving an optimization problem to achieve its Bayesian inference. With the knowledge of this optimization-based learning, the local correlation is incorporated through the pairwise constraint, which integrates an appropriate penalty term into the objective function so as to encourage the neighboring pixels to fall into the same category and to alleviate the “salt-and-pepper” classification appearance. We develop the learning algorithm with all the closed-form updates. The performance of the proposed method is evaluated with both low-resolution and high-resolution PolSAR images, which involve homogeneous, heterogeneous, and extremely heterogeneous areas. The experimental results reveal that the class-dependent texture variable is beneficial to PolSAR image classification and the pairwise constraint can effectively incorporate the local correlation in PolSAR images.

Index Terms—Polarimetric synthetic aperture radar (PolSAR); unsupervised classification; Dirichlet process; variational inference; remote sensing.

I. INTRODUCTION

This work was supported in part by the China Scholarship Council, by the FWO project G037115N: Data Fusion for Image Analysis in Remote Sensing, and by the National Natural Science Foundation of China under Grant 61871335, and by the Frontier Intersection Basic Research Project for the Central Universities under Grant A0920502051814-5. (*Corresponding author: Heng-Chao Li.*)

C. Liu is with the Sichuan Provincial Key Laboratory of Information Coding and Transmission, Southwest Jiaotong University, Chengdu 610031, China, and also with Image Processing and Interpretation, IMEC Research Group at Ghent University, Belgium (e-mail: chi.liu@ugent.be).

H.-C. Li is with the Sichuan Provincial Key Laboratory of Information Coding and Transmission, Southwest Jiaotong University, Chengdu 610031, China (e-mail: lihengchao_78@163.com).

W. Liao and W. Philips are with Image Processing and Interpretation, IMEC Research Group at Ghent University, Belgium (e-mail: wenzhi.liao@ugent.be; wilfried.philips@ugent.be).

W. J. Emery is with the Department of Aerospace Engineering Sciences, University of Colorado at Boulder, Boulder, CO 80309 USA (e-mail: emery@colorado.edu).

CLASSIFICATION plays a significant role in analyzing medical images [1], biological images [2], and remote sensing images [3], [4]. In remote sensing, polarimetric synthetic aperture radar (PolSAR) possesses an advantage in acquiring images: it is less limited by weather conditions or solar illumination due to the active imaging mechanism of PolSAR. Furthermore, with radar waves being emitted and backscattered in different combinations of horizontal and vertical polarization, PolSAR fully captures the scattering properties of targets, which can provide insights into the physical scattering mechanism for a better understanding of terrain types and improve the discriminative ability in the classification of PolSAR images. Unsupervised classification of PolSAR images has been widely used in various applications ranging from man-made target extraction [5], ship detection [6] to glacier monitoring [7] and damage assessment [8].

The H/α -Wishart method [9] is a widely used unsupervised classification method for PolSAR images. It first classifies all pixels into eight classes based on the Cloude-Pottier decomposition [10], and then the Wishart classifier [11] is implemented on the resulting classification map to achieve a refined result. To further improve the discriminative ability, additional parameters have been introduced to identify more details in PolSAR images, such as SPAN (i.e., the total power), the anisotropy information, the scattering power entropy, and the copolarized ratio [12]–[14]. In all these methods, the Wishart classifier is also used to take into account the statistical characteristic of PolSAR data, for which a covariance matrix for PolSAR data follows the complex Wishart distribution [15]–[17]. This statistical characteristic has resulted in several distance measures [18], [19], which are successfully applied in fuzzy clustering methods for the unsupervised classification of PolSAR images [20], [21]. Classification methods based on statistical modeling have also been proposed [18], [22]. These methods first fit a weighted sum of several complex Wishart distributions (i.e., complex Wishart mixture model, which is abbreviated to WMM) to all the data in a PolSAR image. Then, by associating each component in the WMM with a unique category, they achieve the class posterior probability of a PolSAR data point belonging to a category according to Bayes’ theorem, which facilitates the determination of pixel labels for unsupervised classification. However, these complex-Wishart-distribution-based methods cannot always provide reliable classification results for PolSAR data from high-resolution images and in heterogeneous areas, for which

the adopted complex Wishart distribution is not valid any more due to the violation of the *fully developed speckle* condition [16].

One of the important conditions for *fully developed speckle* is that a large number of scatterers should be included in a resolution cell of homogeneous areas [16], which guarantees the validity of the Central Limit Theorem (CLT). Thus, a scattering vector follows the multivariate zero-mean circular Gaussian distribution, and a covariance matrix for PolSAR data is characterized by the complex Wishart distribution. However, with the resolution increase of the PolSAR image, a resolution cell (or pixel) corresponds to a smaller ground area. Thus, for the high-resolution PolSAR images, there are only a limited number of scatterers in a resolution cell, and the effective scatterer number could significantly vary from one pixel to another, leading to the heterogeneity. In this case, the condition for *fully developed speckle* is not fulfilled, which implies that the circular Gaussian distribution and the complex Wishart distribution cannot accurately characterize PolSAR data. This requires non-Gaussian/non-Wishart clutter models for the classification of PolSAR images with high scene heterogeneity [23]–[25]. Non-Gaussian/non-Wishart clutter models for PolSAR data are generally developed with the product model. In the product model, PolSAR data are represented by the product of a complex-Wishart-distributed speckle component and a scalar texture variable [26], [27]. When a distribution has been selected for the scalar texture variable, the joint distribution for the product model can be obtained, from which a compound distribution of observed PolSAR data is further derived by integrating the scalar texture variable out [28]–[33]. The application of compound distributions has demonstrated promising results in PolSAR image classification [34], [35]. Nevertheless, numerical methods are generally required to deal with the complicated functions in the derived compound distributions, which inhibits their potential applications.

In PolSAR image classification, the pixel-wise methods generally provide results with a severe “salt-and-pepper” appearance, which presents a major challenge to the interpretation of PolSAR images. Incorporating the correlation among neighboring pixels contributes to the mitigation of the “salt-and-pepper” effect. To this end, an intuitive solution is to treat regions as the elements of classification. This idea is generally implemented by two main steps, including 1) oversegmentation of a PolSAR image into a large number of regions (patches) or superpixels, and 2) classification of the resulting regions or superpixels [36], [37]. In the region-based methods of this kind, the contextual information is incorporated in the classification step by assigning all the pixels in a region to the same category. The classification performance of the region-based methods are heavily dependent on the segmentation quality of the first step. An inappropriate segmentation could lead to the detail loss in the classification map as well as the significant reduction of the classification accuracy.

To incorporate the spatial interdependencies in the pixel-wise methods, a Markov random field (MRF) is commonly used [38]–[41]. The energy function derived from the MRF has been introduced in a level set method, which effectively encourages the neighboring pixels to have the same labels as

the centered pixel [42]. Moreover, an MRF can be exploited in a post-processing step to perform contextual smoothing [43]. In a recent approach for supervised classification, convolutional neural network (CNN) [44] combines an MRF to enforce the label smoothing [45]. In these methods, the MRF generally requires the explicit modeling of observed data and the imposition of a local prior on labels to model the spatial relations. Then, the class posterior distribution given observations can be inferred so as to determine the pixel labels. By contrast, a conditional random field (CRF) directly considers the class posterior distribution in a discriminative framework, which includes at least the unary potential and the pairwise potential [46], [47]. In literature, the spatial interdependencies are established through the pairwise potential [48], [49]. Wang *et al.* propose an adaptive hybrid CRF model, which defines the pairwise potential based on both the labels of two adjacent superpixels and the similarity of their features [50]. CRF has also been successfully applied in describing the complicated relations among superpixels at multiple scales [51]. The high-order potential beyond the unary and pairwise potentials in the CRF is exploited to model the spatial location cues, which takes into account the nonlocal relations and helps to distinguish confused land-cover types [52].

Similarly to MRF and CRF, the idea of establishing pairwise relationships is also developed in a general manner [53]–[56]. A pairwise term has been defined to encourage label smoothness [57]. In feature extraction for PolSAR image classification, a pairwise constraint imposes the similarity on a data sample and its nearest neighbors [58]. The pairwise constraint can be flexibly introduced into an existing framework to consider the contextual information, leading to an integrated method for PolSAR image classification. This resulting integrated method from the introduction of the pairwise constraint inherently avoids the dependencies between two successive steps, and it is possible to provide good solutions as well as accurate classification results.

In this paper, we propose a textured Dirichlet process mixture model with the pairwise constraint (tDPMM-PC) for unsupervised classification of PolSAR images. To better characterize the heterogeneity in PolSAR data (especially from high-resolution images), we establish the generation procedure of an observed PolSAR data point according to the multiplication representation in the product model. Specifically for the generation procedure, the class-dependent texture variable and the speckle component are first generated according to the inverse Gamma distribution and the complex Wishart distribution, and then an observed PolSAR data point is obtained as the product of these two sampled variables. We further integrate this generation procedure into the framework of the Dirichlet process mixture model (DPMM) [59]–[61] for unsupervised classification, leading to the proposed textured DPMM (tDPMM). In the existing methods, the heterogeneity is characterized in such a vague way that the PolSAR data with high scene heterogeneity are described by a compound distribution derived from the product model. By contrast, the proposed tDPMM explicitly considers the heterogeneity through the integrated texture variable. According to the generation procedure of the tDPMM, its Bayesian model is

formulated, which not only provides the flexibility in modeling PolSAR data, but also eliminates the need to deal with the complicated function involved in the compound distributions. To alleviate the “salt-and-pepper” classification effect, the local correlation is incorporated into the tDPMM through the pairwise constraint, for which a center pixel is paired with all its neighboring pixels. A similarity measure between paired pixels is presented, which facilitates the derivation of the closed-form updates in the learning algorithm and leads to an integrated method. When the penalty term based on the similarity measure is introduced to the objective function (i.e., the lower bound in variational inference [62]), a variational learning algorithm for the proposed tDPMM-PC is conveniently achieved with all the closed-form updates, and the local correlation is incorporated in the inference stage. In particular, according to the resulting update equations, the class-dependent texture variable exhibits the property of adaptively scaling the observed PolSAR data to their own category centers (rather than to a common category center), which implies the robustness of the proposed method to some extent.

This paper is structured as follows. Section II introduces the preliminaries, including the statistical characteristics of PolSAR data and the framework of the Dirichlet process mixture model. In Section III, we deal with the heterogeneity in PolSAR data by proposing a textured Dirichlet process mixture model (tDPMM). Its learning algorithm is developed based on variational inference. Section IV is devoted to incorporating the local correlation into the proposed tDPMM through the pairwise constraint. With variational inference, we derive the closed-form updates for the corresponding variational learning algorithm. Section V demonstrates the experimental results and discussion. Finally, the conclusions of the paper are drawn in Section VI.

II. PRELIMINARIES ON POLSAR DATA MODELING AND DIRICHLET PROCESS MIXTURE MODEL

A. PolSAR Data and Statistical Properties

PolSAR acquires data by emitting and receiving radar waves in different combinations of horizontal polarization (h) and vertical polarization (v). A PolSAR data vector is represented by a complex scattering vector (SV) as [16]

$$\mathbf{S} = [S_{hh}, S_{hv}, S_{vh}, S_{vv}]^T, \quad (1)$$

where the superscript T is the transpose operator. This vector includes amplitude and phase information to represent a target. For a reciprocal medium, the scattering vector reduces to $\mathbf{S} = [S_{hh}, \sqrt{2}S_{hv}, S_{vv}]^T$ under the assumption of $S_{hv} = S_{vh}$.

In PolSAR images, a granular noise pattern is always demonstrated due to the speckle, leading to the difficulty in image interpretation. To reduce this negative effect, multilook PolSAR data are commonly exploited in interpretation tasks. The multilook PolSAR data (e.g., the multilook covariance matrix) are obtained by averaging the covariance matrices of neighboring pixels [15]–[17], i.e.,

$$\mathbf{C} = \frac{1}{L} \sum_{i=1}^L \mathbf{S}_i \mathbf{S}_i^H, \quad (2)$$

where \mathbf{S}_i is the scattering vector in (1), and L is the number of looks. The covariance matrix of a neighboring pixel is evaluated according to $\mathbf{S}_i \mathbf{S}_i^H$, where the superscript H is the Hermitian transpose. This multilook sampling reduces the granular noise pattern in PolSAR images and preserves the polarimetric properties.

In homogeneous areas, this multilook covariance matrix can be characterized by the complex Wishart distribution $\mathcal{W}(\mathbf{C}; L, \Omega^{-1})$ [16], [17]

$$\mathcal{W}(\mathbf{C}; L, \Omega^{-1}) = \frac{L^L d}{\Gamma_d(L)} \frac{|\mathbf{C}|^{L-d}}{|\Omega^{-1}|^L} \exp \left\{ -L \cdot \text{tr}(\Omega \mathbf{C}) \right\}, \quad (3)$$

where d is the number of elements in \mathbf{S}_i , $\Gamma_d(L) = \pi^{\frac{d(d-1)}{2}} \prod_{i=0}^{d-1} \Gamma(L-i)$, and $\Gamma(x) = \int_0^{+\infty} z^{x-1} \exp\{-z\} dz$ is the Gamma function. Ω^{-1} is the expectation of the covariance matrix \mathbf{C} . $|\cdot|$ and $\text{tr}(\cdot)$ evaluate the determinant and the trace, respectively. In statistical-modeling-based methods for the interpretation of PolSAR images, the complex Wishart distribution is the basis for constructing flexible models.

B. Product Model

In high-resolution PolSAR images and heterogeneous areas, the effective scatterer number could vary spatially from one pixel to another one, which leads to the heterogeneity and makes the complex Wishart distribution not valid. In this case, the product model is helpful in developing heterogeneous clutter models for PolSAR data. The product model for PolSAR data decomposes an observed covariance matrix as the product of two independent random variables [27], [30], i.e.,

$$\mathbf{C} = t \cdot \mathbf{Y}, \quad (4)$$

where t is the texture variable, and \mathbf{Y} is the speckle component. The positive and scalar texture variable represents the spatial fluctuation of effective scatterer number from one resolution cell to another [27]. The other random variable (i.e., the speckle component \mathbf{Y}) follows the complex Wishart distribution.

With the help of the complex-Wishart-distributed speckle component \mathbf{Y} in (4), we obtain a conditional probability density function (PDF) of the covariance matrix \mathbf{C} given the texture variable t as [16]

$$p(\mathbf{C}|t, \Omega) = \frac{L^L d}{\Gamma_d(L)} \frac{|\mathbf{C}|^{L-d}}{|\Omega|^{-L} \cdot t^L d} \exp \left\{ -\frac{L \cdot \text{tr}(\Omega \mathbf{C})}{t} \right\}. \quad (5)$$

In this distribution, L is the equivalent number of looks, which can be determined according to the PolSAR data from homogeneous areas. Thus, L can be conveniently treated as a known parameter. Furthermore, given the PDF of the texture variable $p(t)$, the compound distribution of the multilook covariance matrix \mathbf{C} is derived by [26], [27]

$$p(\mathbf{C}; \Omega) = \int p(\mathbf{C}|t, \Omega) \cdot p(t) dt. \quad (6)$$

With this procedure, many flexible models have been yielded to statistically characterize PolSAR data. Nevertheless, the marginalization operation [see (6)] in the product model generally leads to the presence of complicated functions, which inhibits the potential application of the derived models.

C. Dirichlet Process Mixture Model

A realistic PolSAR image always involves various types of regions, which exhibit different scattering characteristics. A unimodal distribution (e.g., a compound distribution derived from the product model) cannot accurately capture all statistical characteristics in a PolSAR image. This limitation can be overcome by the framework of the Dirichlet process mixture model (DPMM), which offers the opportunity to accurately model a PolSAR image with a mixture of distributions and is commonly used in unsupervised classification [60], [61].

The DPMM is formulated as a hierarchical Bayesian model, which is given by [60], [61], [63]

$$G|\alpha, G_0 \sim DP(\alpha, G_0), \quad (7)$$

$$\theta_n|G \sim G, \quad (8)$$

$$x_n|\theta_n \sim p(x_n|\theta_n). \quad (9)$$

This formulation illustrates the generation procedure of an observation.

- 1) Firstly, (7) reveals that the respective probability for each category (component) included in G is generated according to a nonparametric prior, i.e., the Dirichlet process (DP) $DP(\alpha, G_0)$ with the positive concentration parameter α and the base distribution G_0 [59], [64]. When α is a quite small value, only a few categories take high probability, which implies that the observation x_n is only possible to be generated from one of the few categories with high probability. When α is a large value, it is almost equally possible for all the categories to generate observation x_n .
- 2) Subsequently, according to the probability of categories (i.e., G in (7) and (8)), the category to generate observation x_n is determined, which is indicated by θ_n in (8).
- 3) Finally, given the knowledge of which category generates x_n , the observation x_n is sampled from the data distribution $p(x_n|\theta_n)$ in (9), which is associated with the generating category (component).

By repeatedly performing this generation procedure, we can obtain a data set with any given number of observations. For instance, this data set could include the PolSAR data in an image.

The key in the DPMM formulation is to explicitly represent the discrete distribution G from the DP [see (7)]. To this end, the stick-breaking representation [64], [65] is generally adopted, i.e.,

$$\omega_i(\mathbf{v}) = v_i \prod_{j=1}^{i-1} (1 - v_j), \quad (10)$$

$$v_i \sim Beta(v_i; 1, \alpha), \quad (11)$$

$$G = \sum_{i=1}^{\infty} \omega_i(\mathbf{v}) \delta_{(\theta_i^*)}, \quad (12)$$

where $\delta_{(\cdot)}$ is a Dirac delta function. (10)-(12) can be interpreted as a procedure of breaking a unit length “stick”. Starting with a unit length “stick”, the mixing proportion (the category probability) for i -th component $\omega_i(\mathbf{v})$ is obtained by breaking off a portion of the remaining “stick”. In (10), $\prod_{j=1}^{i-1} (1 - v_j)$

is the remaining “stick”, and v_i is the portion for the i -th breaking-off. This breaking portion is determined from the Beta distribution $Beta(v_i; 1, \alpha) = \alpha(1 - v_i)^{\alpha-1}$ in (11). It can be observed from (12) that the mixing proportions are included in the discrete distribution G .

The stick-breaking construction guarantees $\omega_i(\mathbf{v}) > 0$ and $\sum_{i=1}^{\infty} \omega_i(\mathbf{v}) = 1$. The parameter α in (12) (i.e., the concentration parameter in the DP) controls the breaking-off portion of the remaining “stick”. When α is quite small, less portion of the “stick” is left for the next breaking-off, leading to a small number of significant components in the DPMM. Thanks to the introduction of the DP, the DPMM can treat the component number (i.e., the cluster number) as a random variable, and the component number can be determined according to observations [61]. In addition, this stick-breaking representation allows to learn the DPMM with optimization-based inference methods, such as variational inference [62].

III. TEXTURED DPMM FOR POLSAR DATA AND ITS VARIATIONAL INFERENCE

In this section, a textured DPMM (tDPMM) is proposed, which takes into account the heterogeneity in PolSAR data. The Bayesian inference model for the proposed tDPMM is formulated by explicitly introducing the texture variable and by appropriately assigning the observation distribution and the prior distributions.

A. Textured DPMM for PolSAR Data

In the proposed textured DPMM (tDPMM), the class-dependent texture variable is introduced in the DPMM framework to characterize the heterogeneity, and each of observed PolSAR data is described based on the multiplication of the texture variable and the Wishart-distributed component. The Bayesian formation of the proposed tDPMM is given by

$$v_i \sim Beta(v_i; 1, \alpha), \quad (13)$$

$$\omega_i(\mathbf{v}) = v_i \prod_{j=1}^{i-1} (1 - v_j), \quad (14)$$

$$\mathbf{z}_n|\omega(\mathbf{v}) \sim Mul(\mathbf{z}_n; \omega(\mathbf{v})), \quad (15)$$

$$t_n|\mathbf{z}_n \sim p(t_n|\mathbf{z}_n), \quad (16)$$

$$\Omega_{\mathbf{z}_n} \sim p(\Omega_{\mathbf{z}_n}; \theta_{\mathbf{z}_n}), \quad (17)$$

$$C_n|\mathbf{z}_n, t_n \sim p(C_n|\mathbf{z}_n, t_n, \Omega_{\mathbf{z}_n}). \quad (18)$$

The generative process of the proposed tDPMM is similar to that of the DPMM. Firstly, the mixing proportions $\omega(\mathbf{v}) = \{\omega_1(\mathbf{v}), \dots, \omega_{\infty}(\mathbf{v})\}$ for the components are determined according to (13) and (14). Subsequently, based on the mixing proportions, the binary vector $\mathbf{z}_n = [z_{n1}, \dots, z_{n\infty}]$, where only one element equals 1 and the other elements are 0, is sampled according to the multinomial distribution $Mul(\mathbf{z}_n; \omega(\mathbf{v})) = \prod_i \omega_i(\mathbf{v})^{z_{ni}}$ in (15) so as to indicate the component (category) of generating a PolSAR data point C_n . Given the generating component indicated by \mathbf{z}_n , the texture variable t_n and the distribution parameter $\Omega_{\mathbf{z}_n}$ for this component can be obtained as shown in (16) and (17). In the final stage, an observed PolSAR data point C_n is generated

by following the conditional data distribution given the texture variable t_n , the component parameter $\Omega_{\mathbf{z}_n}$, and the indicator variable \mathbf{z}_n .

To apply the proposed tDPMM in unsupervised classification of PolSAR data, the PDF of the texture variable in (16) and the conditional distribution of PolSAR data in (18) are required. Furthermore, a conjugate prior distribution for the variable in the data distribution needs to be determined [see (17)]. We will successively give the selection of these three PDFs. In literature, it has been shown that the inverse Gamma distribution is effective in describing the texture in PolSAR images [29], [66]. Therefore, the inverse Gamma distribution is selected as the PDF of the texture variable, i.e.,

$$p(t_n; a_n, b_n) = \frac{b_n^{a_n}}{\Gamma(a_n)} t_n^{-a_n-1} \exp\left\{-\frac{b_n}{t_n}\right\} \quad (19)$$

where a_n and b_n are the shape parameter and the scale parameter, respectively.

The conditional PDF of the observed PolSAR data is derived based on the multiplicative representation in the product model as shown in (4). Specifically, with the knowledge of the complex-Wishart-distributed speckle component and by performing the transformation from Y_n to C_n , the conditional PDF of the observed PolSAR data C_n given the texture variable t_n is obtained as $p(C_n|t_n, \Omega)$ in (5). For Ω in (5), its conjugate prior is the complex Wishart distribution [67]. If a conjugate prior is assigned in Bayesian inference, the functional form of the corresponding posterior distribution is the same as the prior distribution [62]. With this knowledge about the conjugate prior, the derivation of the posterior distribution could be significantly simplified.

Once the proposed tDPMM has been learned, the unsupervised classification of PolSAR data can be achieved by assigning each data point to a label according to the largest element in the expectation of the category-indicator vector [68], [69], i.e.,

$$l_n = \arg \max_i \mathbf{E}[z_{ni}], \quad (20)$$

where l_n is the label for data point n , and $\mathbf{E}[\cdot]$ performs the expectation.

B. Variational Inference for the Textured DPMM

The learning algorithm for the proposed tDPMM is developed based on variational inference. We will first present the basic idea of variational inference and then focus on the derivation of the update equations in the variational learning algorithm for the proposed tDPMM.

In variational inference, the general idea is to maximize the variational lower bound $\mathcal{L}(q(\Lambda))$ with respect to the posterior distribution so as to obtain the solution [62], i.e.,

$$q^* = \arg \max_{q(\Lambda)} \mathcal{L}(q(\Lambda)), \quad (21)$$

where $\mathcal{L}(q(\Lambda)) \triangleq \int q(\Lambda) \ln \frac{p(\mathbf{C}, \Lambda)}{q(\Lambda)} d\Lambda$. \mathbf{C} and Λ are respectively the set of observations and the set of all random variables. Specifically for the tDPMM, $\mathbf{C} = \{C_1, \dots, C_N\}$ is the set of all the observations in a PolSAR image and Λ includes all the variables $\mathbf{Z} = \{\mathbf{z}_n\}$, \mathbf{v} , $\mathbf{t} = \{t_n\}$,

and $\Omega = \{\Omega_{\mathbf{z}_n}\}$. Λ does not involve $\omega(\mathbf{v})$, since $\omega_i(\mathbf{v})$ is evaluated based on \mathbf{v} according to (14).

In practice, the true posterior distribution $p(\Lambda|\mathbf{C})$ is generally not tractable. An idea to obtain tractable solution is to approximate the posterior distribution by breaking the dependencies among the random variables. To this end, the fully factorized approximation based on the mean field theory is generally exploited, which factorizes the posterior distribution into disjoint groups $q(\Lambda) = \prod_i q(\Lambda_i)$ and opens the possibility of achieving tractable solutions [70]. With this approximation, the solution to the maximization problem in (21) can be derived in element-wise form as [62]

$$q^*(\Lambda_i) = \frac{\exp\{\mathbf{E}_{j \neq i}[\ln p(\mathbf{C}, \Lambda)]\}}{\int \exp\{\mathbf{E}_{j \neq i}[\ln p(\mathbf{C}, \Lambda)]\} d\Lambda_i}, \quad (22)$$

where $\mathbf{E}_{j \neq i}[\ln p(\mathbf{C}, \Lambda)] = \int \ln p(\mathbf{C}, \Lambda) \prod_{j \neq i} q(\Lambda_j) d\Lambda_j$ performs the integration over every Λ_j except for $j = i$ and only keeps the desired Λ_i . The integration in the denominator is a normalization term that guarantees the solution in (22) to be probabilistic. It is worth noting that when a conjugate prior is assigned for each Λ_i , the posterior distribution $q^*(\Lambda_i)$ can be conveniently achieved by matching the form of the prior distribution with the corresponding posterior distribution [62].

Based on the variational inference aforementioned, we develop the variational learning algorithm for the proposed tDPMM. The log-likelihood function for the proposed tDPMM is represented by

$$\begin{aligned} \ln p(\mathbf{C}, \Lambda) \\ = \ln p(\mathbf{C}|\mathbf{Z}, \mathbf{t}, \Omega) + \ln p(\mathbf{t}|\mathbf{Z}) + \ln p(\mathbf{Z}|\omega(\mathbf{v})) \\ + \ln p(\mathbf{v}; \alpha_0) + \ln p(\Omega; \{\theta_{i0}\}), \end{aligned} \quad (23)$$

where $\Lambda = \{\mathbf{Z}, \mathbf{v}, \mathbf{t}, \Omega\}$, and the prior distribution $p(\Omega; \{\theta_{i0}\})$ is introduced for the fully Bayesian formulation of the inference model. To achieve tractable solutions with variational inference, the true posterior distribution $p(\Lambda|\mathbf{C})$ is approximated as

$$p(\Lambda|\mathbf{C}) \approx q(\Lambda) = q(\Omega)q(\mathbf{v})q(\mathbf{t}|\mathbf{Z})q(\mathbf{Z}). \quad (24)$$

For this approximation, we consider a structural factorization between the texture variable \mathbf{t} and the indicator variable \mathbf{Z} , rather than breaking all the dependencies.

As elaborated in Section III.A, the distributions involved in (23) are detailed as follows:

$$p(\mathbf{C}|\mathbf{Z}, \mathbf{t}, \Omega) = \prod_n \prod_i \left\{ p(C_n|t_n, \Omega_i) \right\}^{z_{ni}}, \quad (25)$$

$$p(\mathbf{t}|\mathbf{Z}) = \prod_n \prod_i \left\{ p(t_n; a_{ni0}, b_{ni0}) \right\}^{z_{ni}}, \quad (26)$$

$$p(\mathbf{Z}|\omega(\mathbf{v})) = \prod_n \prod_i \left\{ v_i \prod_{j=1}^{i-1} (1 - v_j) \right\}^{z_{ni}}, \quad (27)$$

$$p(\mathbf{v}; \alpha_0) = \prod_i \alpha_0 (1 - v_i)^{\alpha_0 - 1}, \quad (28)$$

$$p(\Omega; \{\eta_{i0}, W_{i0}^{-1}\}) = \prod_i \mathcal{W}(\Omega_i; \eta_{i0}, W_{i0}^{-1}), \quad (29)$$

where $p(C_n|t_n, \Omega_i)$ can be found from (5) and $p(t_n; a_{ni0}, b_{ni0})$ from (19). The PDF for the indicator

variable $\mathbf{Z} = \{z_n\}$ in (27) is obtained by substituting (14) into (15). By substituting these distributions into (23), the log-likelihood function is found to be

$$\begin{aligned} \ln p(\mathbf{C}, \mathbf{\Lambda}) &= \sum_n \sum_i z_{ni} \left\{ \ln \frac{L^{Ld}}{\Gamma_d(L)} + (L-d) \ln |C_n| + L \ln |\Omega_i| \right. \\ &\quad \left. - Ld \ln t_n - \frac{L}{t_n} \cdot \text{tr}(\Omega_i C_n) \right\} + \sum_i (\alpha_0 - 1) \ln(1 - v_i) \\ &\quad + \sum_n \sum_i z_{ni} \left\{ \ln \frac{b_{ni0}^{a_{ni0}}}{\Gamma(a_{ni0})} - (a_{ni0} + 1) \cdot \ln t_n - \frac{b_{ni0}}{t_n} \right\} \\ &\quad + \sum_n \sum_i z_{ni} \left\{ \ln v_i + \sum_{j=1}^{i-1} \ln(1 - v_j) \right\} \\ &\quad + \sum_i \left\{ (\eta_{i0} - d) \ln |\Omega_i| - \eta_{i0} \cdot \text{tr}(W_{i0} \Omega_i) \right\} + \text{const}, \end{aligned} \quad (30)$$

where ‘‘const’’ is the summation of all the independent terms of $\mathbf{\Lambda}$.

Based on (30) and following the variational inference, we obtain the posterior distributions, i.e., $q(\mathbf{Z})$, $q(\mathbf{v})$, $q(\mathbf{\Omega})$, and $q(\mathbf{t}|\mathbf{Z})$ in (24). The posterior distribution of the variable $\mathbf{Z} = \{z_n\}$ is given in logarithm as

$$\ln q^*(\mathbf{Z}) = \sum_n \sum_i z_{ni} \ln r_{ni}, \quad (31)$$

where $\mathbf{E}[z_{ni}] = r_{ni}$ and $r_{ni} = \rho_{ni} / \sum_j \rho_{nj}$. ρ_{ni} is evaluated by taking the exponential of

$$\begin{aligned} \ln \rho_{ni} &= \ln \frac{L^{Ld}}{\Gamma_d(L)} + \ln \frac{b_{ni0}^{a_{ni0}}}{\Gamma(a_{ni0})} + L \mathbf{E}[\ln |\Omega_i|] \\ &\quad + (L-d) \ln |C_n| - (a_{ni0} + Ld + 1) \cdot \mathbf{E}_{z_{ni}}[\ln t_n] \\ &\quad - (b_{ni0} + L \cdot \text{tr}(\mathbf{E}[\Omega_i] C_n)) \cdot \mathbf{E}_{z_{ni}}\left[\frac{1}{t_n}\right] + \mathbf{E}[\ln \omega_i(\mathbf{v})], \end{aligned} \quad (32)$$

where $\mathbf{E}[\ln \omega_i(\mathbf{v})] = \mathbf{E}[\ln v_i] + \sum_{j=1}^{i-1} \mathbf{E}[\ln(1 - v_j)]$ and $\mathbf{E}[\cdot]$ performs the expectation over the posterior distribution. $\mathbf{E}_{z_{ni}}[\cdot]$ is the conditional expectation given $z_{ni} = 1$. The posterior distribution in (31) provides the possibility information of the a PolSAR data point C_n belonging to the i -th component (category) in view of both $\mathbf{E}[z_{ni}] = r_{ni}$ and the expression of r_{ni} , which facilitates the classification of a PolSAR image.

The posterior distributions for each v_i and each Ω_i are respectively the Beta distribution and the complex Wishart distribution in view of the introduced conjugate priors. Their posterior distributions in logarithm are presented as

$$\begin{aligned} \ln q^*(\mathbf{v}) &= \sum_i \left\{ (\beta_i - 1) \ln v_i + (\alpha_i - 1) \ln(1 - v_i) \right\} + \text{const} \\ &= \sum_i \left\{ (\alpha_0 + \sum_{j=i+1}^{\infty} \sum_n \mathbf{E}[z_{nj}] - 1) \cdot \ln(1 - v_i) \right. \\ &\quad \left. + \sum_n \mathbf{E}[z_{ni}] \cdot \ln v_i \right\} + \text{const}, \end{aligned} \quad (33)$$

and

$$\begin{aligned} \ln q^*(\mathbf{\Omega}) &= \sum_i \left\{ (\eta_i - d) \cdot \ln |\Omega_i| - \eta_i \cdot \text{tr}(W_{i0} \Omega_i) \right\} + \text{const} \\ &= \sum_i \left\{ (\eta_{i0} + L \sum_n \mathbf{E}[z_{ni}] - d) \cdot \ln |\Omega_i| \right. \\ &\quad \left. - \text{tr}([\eta_{i0} W_{i0} + L \sum_n \mathbf{E}[z_{ni}] \mathbf{E}_{z_{ni}}\left[\frac{1}{t_n}\right] \cdot C_n] \cdot \Omega_i) \right\} \\ &\quad + \text{const}. \end{aligned} \quad (34)$$

Similarly, the solution to the texture variable \mathbf{t} is given by

$$\begin{aligned} \ln q^*(\mathbf{t}|\mathbf{Z}) &= \sum_n \sum_i z_{ni} \left\{ - (a_{ni} + 1) \cdot \ln t_n - \frac{b_{ni}}{t_n} \right\} + \text{const} \\ &= \sum_n \sum_i z_{ni} \left\{ - (a_{ni0} + Ld + 1) \cdot \ln t_n \right. \\ &\quad \left. - [b_{ni0} + L \cdot \text{tr}(\mathbf{E}[\Omega_i] C_n)] \cdot \frac{1}{t_n} \right\} + \text{const}, \end{aligned} \quad (35)$$

where the term in the curly brackets takes the form of the inverse Gamma distribution.

The derived posterior distributions and their corresponding prior distributions have the same functional form (e.g., (34) and (29) are the complex Wishart distributions), which implies that the conjugate priors have been assigned in view of the definition [62]. Thus, the update equations for the parameters in the posterior distributions can be conveniently achieved as

$$\beta_i = 1 + \sum_n \mathbf{E}[z_{ni}], \quad (36a)$$

$$\alpha_i = \alpha_0 + \sum_{j=i+1}^{\infty} \sum_n \mathbf{E}[z_{nj}], \quad (36b)$$

$$\eta_i = \eta_{i0} + L \sum_n \mathbf{E}[z_{ni}], \quad (36c)$$

$$W_i = \frac{1}{\eta_i} \left\{ \eta_{i0} W_{i0} + L \sum_n \mathbf{E}[z_{ni}] \mathbf{E}_{z_{ni}}\left[\frac{1}{t_n}\right] C_n \right\}, \quad (36d)$$

$$a_{ni} = a_{ni0} + Ld, \quad (36e)$$

$$b_{ni} = b_{ni0} + L \cdot \text{tr}(\mathbf{E}[\Omega_i] \cdot C_n). \quad (36f)$$

The expected values involved in learning the tDPMM are calculated by

$$\begin{aligned} \mathbf{E}[z_{ni}] &= r_{ni}, \quad \mathbf{E}_{z_{ni}}\left[\frac{1}{t_n}\right] = \frac{a_{ni}}{b_{ni}}, \quad \mathbf{E}[\Omega_i] = W_i^{-1}, \\ \mathbf{E}_{z_{ni}}[\ln t_n] &= \ln b_{ni} - \psi(a_{ni}), \\ \mathbf{E}[\ln v_i] &= \psi(\beta_i) - \psi(\alpha_i + \beta_i), \\ \mathbf{E}[\ln(1 - v_i)] &= \psi(\alpha_i) - \psi(\alpha_i + \beta_i), \\ \mathbf{E}[\ln |\Omega_i|] &= \ln |W_i^{-1}| - d \ln \eta_i + \sum_{j=0}^{d-1} \psi(\eta_i - j), \end{aligned} \quad (37)$$

where $\psi(x) = d \ln \Gamma(x) / dx$ is the digamma function. By alternatively evaluating (31), (32), and (36a)-(36f) until the stop criterion is reached, the proposed tDPMM can be learned and the classification can be performed according to (20).

The inverse-Gamma-distributed texture variable t_n plays a significant role in the proposed tDPMM. Since this texture variable depends on categories and on PolSAR data as shown in its conditional posterior of (35), it is possible to scale multiple PolSAR data towards their own components (categories) rather than a common component. In addition, in view that the learning algorithm iteratively updates the indicator variables \mathbf{Z} and component parameters, the category-dependent texture variable has to be updated in each iteration so as to achieve the appropriate scaling value. Specifically, the expectation $\mathbf{E}_{z_{ni}}[1/t_n]$ in (37) is evaluated based on a_{ni} in (36e) and b_{ni} in (36f). When both a_{ni0} and b_{ni0} in (36e) and (36f) are far smaller than the other terms, then $\mathbf{E}_{z_{ni}}[1/t_n] \rightarrow d/\text{tr}(\mathbf{E}[\Omega_i] \cdot C_n)$, where d is the number of rows in the squared matrix of a PolSAR data point C_n . Thus, in view of the relation $C_n/t_n = Y_n$, $\mathbf{E}_{z_{ni}}[1/t_n]$ can be viewed as a scale factor determined according to the divergence measure $d/\text{tr}(\mathbf{E}[\Omega_i] \cdot C_n)$. When the observed PolSAR data point C_n is “far” away from the i -th cluster center $\mathbf{E}[\Omega_i]$, the value of $\mathbf{E}_{z_{ni}}[1/t_n]$ is small. Consequently, all the observed PolSAR data can be adaptively scaled towards their own components by their unique texture variables so that the complex Wishart distribution for each component can be better exploited to describe the texture-dependent observations [see (18)]. This also illustrates the robustness of the proposed tDPMM to some extent.

Another observation is the marginal posterior distribution of the texture variable t_n , i.e.,

$$q(t_n) = \sum_{\mathbf{z}_n} q(t_n, \mathbf{z}_n) = \sum_i q(t_n | z_{ni}) q(z_{ni}), \quad (38)$$

where $q(z_{ni}) > 0$ and $\sum_i q(z_{ni}) = 1$. This marginal distribution demonstrates that the structural factorization between t and \mathbf{Z} [see (24)] leads to a mixture model for describing the texture variable. This reveals the flexibility of the proposed tDPMM in the statistical modeling task.

IV. TEXTURED DPMM WITH PAIRWISE CONSTRAINT AND ITS VARIATIONAL INFERENCE

In classification results of PolSAR images, pixel-wise methods generally lead to the “salt-and-pepper” appearance, which brings difficulty in visual interpretation. To alleviate the “salt-and-pepper” effect and achieve better results, the proposed tDPMM further incorporates local correlation through the pairwise constraint. We develop the corresponding learning algorithm for this tDPMM with the pairwise constraint (tDPMM-PC) based on the variational inference.

A. Pairwise Constraint for the tDPMM

Local correlation can be described by pairwise relations between a pixel and its neighbors, which reflects prior knowledge about whether two pixels belong to the same class or not. Thus, the idea of pairwise constraint [53]–[55] is applicable in incorporating local correlation. Pairwise constraint has been successfully used in various applications and has demonstrated improved performances [56], [71]–[73]. Compared with the use of the MRF in taking local correlation into account,

the imposition of pairwise constraint is not restricted to the discrete labels. Moreover, exploiting an appropriate measure in pairwise constraint could lead to an integrated method, which facilitates the development of learning algorithm and provide good solutions.

In a local area of an image, when a center pixel is paired with its neighboring pixels, they are assumed to represent similar objects such that a local correlation is established. To quantify the relation between two paired pixels, a similarity measure is presented based on a probability vector $\mathbf{p}_n = [p_{n1}, \dots, p_{ni}, \dots]$, where each element represents the probability of pixel n belonging to cluster i , i.e.,

$$p_{ni} = \frac{\omega_i(\mathbf{v}) \cdot p(C_n | t_n, \Omega_i)}{\sum_i \omega_i(\mathbf{v}) \cdot p(C_n | t_n, \Omega_i)}, \quad (39)$$

where $\omega_i(\mathbf{v}) = v_i \prod_{j=1}^{i-1} (1 - v_j)$ and $p(C_n | t_n, \Omega_i)$ takes the form of (5). The probability vector \mathbf{p}_n includes the information for the classification. Thus, a symmetric similarity measure for two paired pixels n and m is given by

$$f_{nm} = \frac{1}{2} \int q(\Lambda) \left\{ \sum_i (z_{ni} \ln \frac{p_{ni}}{p_{mi}} + z_{mi} \ln \frac{p_{mi}}{p_{ni}}) \right\} d\Lambda. \quad (40)$$

When the probability representations for the paired pixels n and m are exactly the same (i.e., $\mathbf{p}_n = \mathbf{p}_m$), $f_{nm} = 0$. This symmetric similarity measure is an approximation to $\frac{1}{2} \int q(\Lambda) \left\{ \sum_i (p_{ni} \ln \frac{p_{ni}}{p_{mi}} + p_{mi} \ln \frac{p_{mi}}{p_{ni}}) \right\} d\Lambda$ in view of the fact that both p_{ni} and $\mathbf{E}[z_{ni}]$ represent the probability of pixel n belonging to cluster i . More importantly, with the symmetric similarity measure in (40), the local correlation is incorporated in the inference stage, and the closed-form updates can be conveniently derived for the variational learning algorithm.

B. Variational Inference

By introducing a penalty term based on (40), the variational inference for the tDPMM with the pairwise constraint (tDPMM-PC) is performed by solving the following problem

$$\max_{q(\Lambda)} \int q(\Lambda) \ln \frac{p(\mathbf{C}, \Lambda)}{q(\Lambda)} d\Lambda - \sum_n \sum_{m \in \mathcal{N}_n} \gamma_{nm} f_{nm}, \quad (41)$$

where the first term includes the information to individually determine the label of each PolSAR data point. The second term describes the relation between the centered pixel and its neighbors, and it encourages all the pixels in a local area to fall into the same category. \mathcal{N}_n includes pixel n and its neighbors (i.e., the paired pixels). $\gamma_{nm} = 1/\mathfrak{N}(\mathcal{N}_n)$ for $m \in \mathcal{N}_n$, where $\mathfrak{N}(\mathcal{N}_n)$ evaluates the number of pixels in \mathcal{N}_n .

The term $\int q(\Lambda) \ln p(\mathbf{C}, \Lambda) d\Lambda$ can be obtained based on (30), which is in the form of a summation. This summation form is the same as the penalty term [see (40) and the second term in (41)]. Thus, the penalty term can be absorbed by the numerator of the variational lower bound in (41). Let $\int q(\Lambda) \ln \mathcal{J}(\mathbf{C}, \Lambda) d\Lambda = \int q(\Lambda) \ln p(\mathbf{C}, \Lambda) d\Lambda - \sum_n \sum_{m \in \mathcal{N}_n} \gamma_{nm} f_{nm}$. Then, we can learn the proposed tDPMM-PC according to

$$\max_{q(\Lambda)} \int q(\Lambda) \ln \frac{\mathcal{J}(\mathbf{C}, \Lambda)}{q(\Lambda)} d\Lambda. \quad (42)$$

The objective function in this optimization problem keeps the same form as that of the variational inference [see (21)], which implies that the principle of variational inference is still applicable in this problem.

Following the variational inference and with the same structural factorization as (24), the update equations are conveniently obtained for learning the tDPMM-PC as

$$\beta_i = 1 + \sum_n \mathbf{E}[z_{ni}], \quad (43a)$$

$$\alpha_i = \alpha_0 + \sum_{j=i+1}^{\infty} \sum_n \mathbf{E}[z_{nj}], \quad (43b)$$

$$\eta_i = \eta_{i0} + L \sum_n \mathbf{E}[z_{ni}], \quad (43c)$$

$$W_i = \frac{1}{\eta_i} \left\{ \eta_{i0} W_{i0} + L \sum_n \sum_{m \in \mathcal{N}_n} \mathbf{E}[z_{ni}] \gamma_{nm} C_m \mathbf{E}_{z_{mi}} \left[\frac{1}{t_m} \right] \right\}, \quad (43d)$$

$$a_{ni} = a_{ni0} + g_{ni} L d, \quad (43e)$$

$$b_{ni} = b_{ni0} + g_{ni} L \cdot \text{tr}(\mathbf{E}[\Omega_i] \cdot C_n) \quad (43f)$$

$$r_{ni} = \frac{\rho_{ni}}{\sum_j \rho_{nj}}, \quad (43g)$$

where g_{ni} and the logarithm of ρ_{ni} take the form of

$$g_{ni} = \gamma_{nn} + \sum_{m \in \mathcal{N}_n, m \neq n} \gamma_{nm} \mathbf{E}[z_{mi}] \quad (44)$$

and

$$\begin{aligned} \ln \rho_{ni} &= \ln \frac{L^{Ld}}{\Gamma_d(L)} + \frac{b_{ni0}^{a_{ni0}}}{\Gamma(a_{ni0})} + L \mathbf{E}[\ln |\Omega_i|] + \mathbf{E}[\ln \omega_i(\mathbf{v})] \\ &+ (L-d) \sum_{m \in \mathcal{N}_n} \gamma_{nm} \ln |C_m| \\ &- Ld \cdot \left\{ \sum_{m \in \mathcal{N}_n} \gamma_{nm} \mathbf{E}_{z_{mi}} [\ln t_m] \right\} \\ &- L \cdot \text{tr} \left(\mathbf{E}[\Omega_i] \cdot \left\{ \sum_{m \in \mathcal{N}_n} \gamma_{nm} C_m \mathbf{E}_{z_{mi}} \left[\frac{1}{t_m} \right] \right\} \right) \\ &- (a_{ni0} + 1) \mathbf{E}_{z_{ni}} [\ln t_n] - b_{ni0} \mathbf{E}_{z_{ni}} \left[\frac{1}{t_n} \right]. \end{aligned} \quad (45)$$

Here, $\mathbf{E}[\ln \omega_i(\mathbf{v})] = \mathbf{E}[\ln v_i] + \sum_{j=1}^{i-1} \mathbf{E}[\ln(1-v_j)]$ and $\text{tr}(\cdot)$ is the trace operator. The corresponding posterior distributions are given by

$$q^*(\mathbf{v}) = \prod_i \frac{\Gamma(\beta_i + \alpha_i)}{\Gamma(\beta_i)\Gamma(\alpha_i)} v_i^{\beta_i-1} (1-v_i)^{\alpha_i-1}, \quad (46)$$

$$q^*(\Omega) = \prod_i \mathcal{W}(\Omega_i; \eta_i, W_i^{-1}), \quad (47)$$

$$q^*(\mathbf{t}|\mathbf{Z}) = \prod_n \prod_i \left\{ \frac{b_{ni}^{a_{ni}}}{\Gamma(a_{ni})} t_n^{-a_{ni}-1} \exp\left\{-\frac{b_{ni}}{t_n}\right\} \right\}^{z_{ni}}, \quad (48)$$

$$q^*(\mathbf{Z}) = \prod_n \prod_i r_{ni}^{z_{ni}}. \quad (49)$$

By observing (43d)-(43f), these update equations for learning the textured Dirichlet process mixture model with the pairwise constraint (tDPMM-PC) are quite different from

Algorithm 1 Variational Learning Algorithm for the Proposed tDPMM-PC.

- 1: $M \leftarrow$ truncation level.
 - 2: $\{\alpha_0, \eta_{i0}, W_{i0}, a_{ni0}, b_{ni0}\} \leftarrow$ initial values of the hyperparameters in the prior distributions.
 - 3: $\mathbf{E}[\mathbf{Z}] \leftarrow$ initial expectation of the indicator variable.
 - 4: $\{\mathbf{E}_{z_{ni}}[\frac{1}{t_n}], \mathbf{E}_{z_{ni}}[\ln t_n]\} \leftarrow$ initial expected values related to the introduced texture variable \mathbf{t} .
 - 5: $k \leftarrow 0$
 - 6: **while** Stop criterion is not satisfied, **do**
 - 7: Evaluate $\beta_i^{(k+1)}$ and $\alpha_i^{(k+1)}$ by (43a) and (43b)
 - 8: Evaluate $\eta_i^{(k+1)}$ by (43c)
 - 9: Evaluate $W_i^{(k+1)}$ by (43d)
 - 10: Evaluate $a_{ni}^{(k+1)}$ and $b_{ni}^{(k+1)}$ by (43e) and (43f)
 - 11: Update $\mathbf{E}[z_{ni}]^{(k+1)}$ according to (43g) and (45)
 - 12: $k \leftarrow k + 1$
 - 13: $\Theta^{(k)} \leftarrow \{\beta_i^{(k)}, \alpha_i^{(k)}, \eta_i^{(k)}, W_i^{(k)}, a_{ni}^{(k)}, b_{ni}^{(k)}\}$
 - 14: **end while**
 - 15: Output $\Theta^* \leftarrow \Theta^{(k)}$
 - 16: Return $\mathbf{E}[z_{ni}]^{(k)}$
-

those for tDPMM [see (36d)-(36f)], revealing that the local correlation is incorporated through the pairwise constraint.

The complete learning algorithm for tDPMM-PC is illustrated in Algorithm 1, where the truncated stick-breaking representation [61] is exploited. The truncated stick-breaking representation is a standard technique to make the optimization-based variational inference feasible in spite of the infinite number of components [74]. In this truncated stick-breaking representation, the truncation level M is fixed, leading to $p(v_M = 1) = 1$. $p(v_M = 1) = 1$ implies that the M -th breaking takes all the remaining ‘‘stick’’, and we have the mixing coefficients $\omega_j(\mathbf{v}) = 0$ for $j > M$. Thus, only the parameters in a finite number of components (i.e., the component with index j , $j \leq M$) need to be estimated, rather than directly dealing with an infinite number of components.

C. Complexity Analysis

In the proposed algorithm [see Algorithm 1], all the equations (i.e., (43a)-(43g), (44), (45), and (37)) are updated in every iteration. Evaluations for $\ln \rho_{ni}$ in (45), W_i in (43d), and b_{ni} in (43f) cost much more time in view of both the many terms and the manipulation on the neighboring pixels. We focus on the analysis of these three updates since they are the main sources for the complexity of the algorithm.

To update $\ln \rho_{ni}$ in (45), evaluations are performed on the matrix inversion in $\mathbf{E}[\Omega_i]$, the determinant in $\mathbf{E}[\ln |\Omega_i|]$, and the trace. More importantly, it involves the manipulation on the neighboring pixels, which contributes much to the complexity of updating $\ln \rho_{ni}$. Thus, updating $\ln \rho_{ni}$ for all n and i requires the complexity of the order $\mathcal{O}(\ell N M S d^2)$ when $M \ll N$. Here, M is the truncation level, N is the number of observed PolSAR data, d^2 is the number of entries for each PolSAR data point, ℓ is the number of iterations, and $\mathcal{S} = \mathfrak{N}(\mathcal{N}_n)$ is the number of pixels in a local area \mathcal{N}_n centered at pixel n . For W_i , the computation for

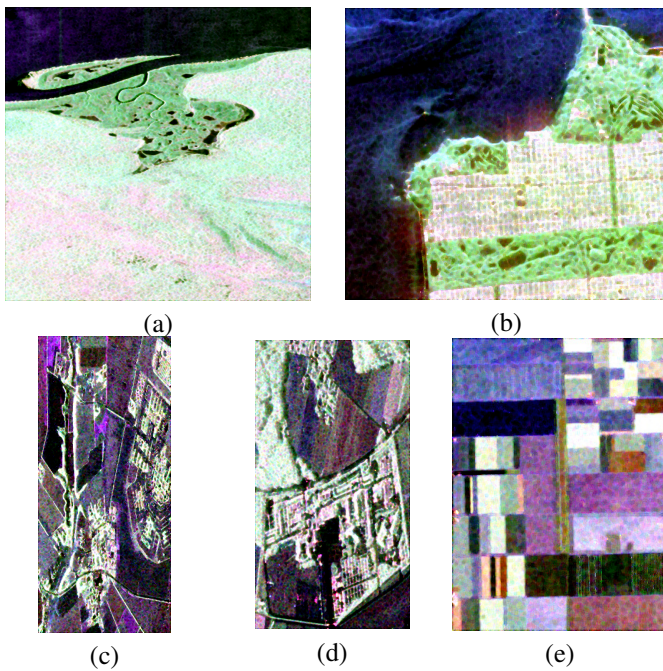


Fig. 1. The Pauli RGB images over the test sites. (a) This is an excerpt of the L-band PolSAR image with the size of 792×827 acquired by NASA/JPL AIRSAR over the savanna area in the north of Kakadu NT, Australia. Its nominal range and azimuth pixel spacing (range \times azimuth in meter) is approximately $6m \times 12m$. (b) An L-band PolSAR image with the size of 479×529 was acquired by NASA/JPL AIRSAR over San Francisco. Its resolution is approximately $10m \times 10m$. (c) A 475×213 PolSAR image was acquired by EMISAR over Foulum, Denmark. This data set is collected in L band, with the nominal range and azimuth pixel spacing (range \times azimuth in meter) of $1.49m \times 0.75m$. (d) An L-band PolSAR image with the size of 787×421 was acquired by DLR ESAR over Oberpfaffenhofen, Germany. Its resolution is approximately $1.5m \times 1.5m$. (e) This is a 383×281 excerpt of the L-band PolSAR image over the agriculture area in Flevoland measured by NASA/JPL AIRSAR. Its nominal range and azimuth pixel spacing (range \times azimuth in meter) is approximately $6m \times 12m$.

the multiplication between a scalar and a $d \times d$ complex-valued matrix C_m performs $2d^2$ multiplications in total on the real part and the imagery part. By further considering the manipulation for all the neighboring pixels, the complexity of updating all W_i is of the order $\mathcal{O}(\ell N M S d^2)$ as well. For all b_{ni} in (43f), the neighboring pixels are manipulated according to (44) and the trace is evaluated for each observation, leading to the complexity of the order $\mathcal{O}(\ell N M (S + d^2))$. Based on the respective analysis for the complexity of the three updates, the total complexity for the learning algorithm is of the order $\mathcal{O}(\ell N M (S d^2 + S + d^2))$.

V. EXPERIMENTAL RESULTS AND DISCUSSION

To verify the effectiveness of the proposed method (i.e., the variational tDPMM-PC method in Section IV), the experiments are performed based on five PolSAR images as shown in Fig. 1. These data sets are acquired by different sensors (e.g., AIRSAR, EMISAR, and DLR ESAR), which facilitate the validation of the proposed method for low-resolution and high-resolution PolSAR images. Moreover, these data sets include various objects and areas of interest including ocean, buildings, woodland, urban areas, and agricultural areas. With these data sets, we can extensively test the proposed method (i.e., the

variational tDPMM-PC method in Section IV) for PolSAR data in homogeneous areas (e.g., ocean), heterogeneous areas (e.g., forest and woodland), and extremely heterogeneous areas (e.g., urban areas).

In Fig. 1, the data sets are respectively referred to as “Kakadu”, “San Francisco”, “Foulum”, “Oberp” short for “Oberpfaffenhofen”, and “Flevoland” according to their place names. These PolSAR images are preprocessed by the refined Lee filter [75]. To explore the separate effects of the introduced texture variable and the pairwise constraint in the proposed method, we present the results for three unsupervised methods, i.e., the variational Dirichlet process mixture of Wishart (i.e., the variational DPMM in Appendix), the variational tDPMM [see Section III], and the proposed method (i.e., the variational tDPMM-PC method in Section IV). With data sets “Kakadu” and “San Francisco”, we evaluate the performance of the proposed method for low-resolution PolSAR images. Similarly, the high-resolution PolSAR images (i.e., data sets “Foulum” and “Oberp”) are used to test the proposed method. Finally, based on data set “Flevoland”, we present the application of the proposed method in the crop classification.

In all the experiments, we use the 5×5 neighborhood. The truncation level is set to the number of categories by default. Otherwise, we will clearly indicate the truncation level. The prior parameters in the proposed method are mostly fixed as $\alpha_0 = 0.1$, $\eta_{i0} = 5$, $a_{ni0} = 10$, and $b_{ni0} = 9$ for all i and n . The selection of W_{i0} depends on data sets.

In addition to the proposed method, the compared methods include another four unsupervised methods and one supervised method. The supervised method is based on the CNN, which directly adopts the complex-valued data as inputs. This complex-valued CNN (CV-CNN) method is suitable for PolSAR data, and it has shown good performance in PolSAR image classification [76]. The unsupervised methods are the H/α -Wishart-MRF method, the Chernoff-Wishart-MRF method, the variational DPMM-MRF method, and the variational tDPMM-MRF method. In H/α -Wishart-MRF method and the Chernoff-Wishart-MRF method, a Markov random field (MRF) prior is introduced into the H/α -Wishart method [9] and the Chernoff-Wishart method [19]. The variational DPMM-MRF method is obtained by combining the variational DPMM [see Appendix] with the MRF as that in [69]. Similarly, we also obtain the variational tDPMM-MRF method so that we can verify the effectiveness of the introduced texture variable by comparing with the variational DPMM-MRF and the effectiveness of the pairwise constraint in the proposed tDPMM-PC by comparing with the MRF. For a fair comparison with the proposed method, all these compared methods have incorporated the contextual information. For quantitative analysis, it is required for these unsupervised classification methods to appropriately associate the generated labels with ground truth labels. To this end, we exhaustively try all the mappings from the generated labels to the ground truth labels and select the mapping with the highest overall accuracy (OA) so as to give the color maps. These methods are quantitatively compared according to the producer’s accuracy, OA, and the kappa coefficient (κ). In every table of the accuracy assessment, the column for the CV-CNN method

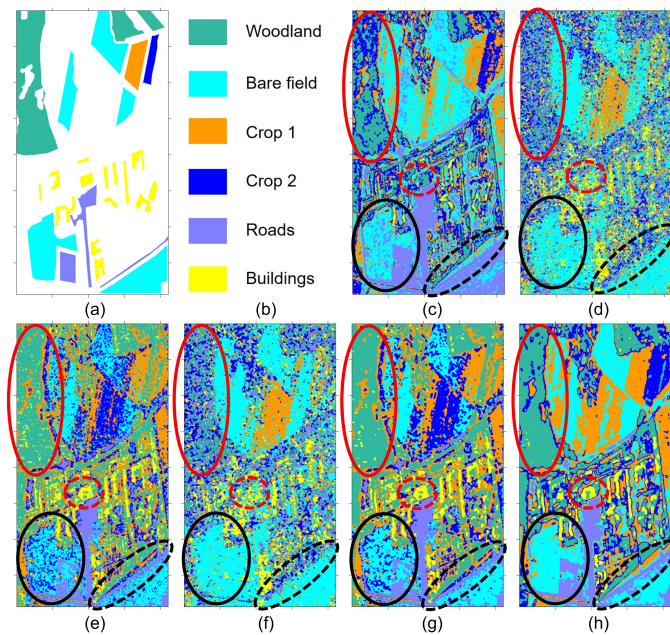


Fig. 2. The ground truth for data set ‘‘Oberp’’ and the classification maps for ablation studies. (a) The ground truth. (b) The legend. (c) The variational DPMM. (d) The procedure of ‘‘Scaling+DPMM’’. (e) Our tDPMM. (f) The procedure of ‘‘Scaling+DPMM+MF’’. (g) The procedure of ‘‘tDPMM+MF’’. (h) The proposed method.

TABLE I
ACCURACY ASSESSMENT FOR THE EFFECTS OF THE TEXTURE VARIABLE AND THE PAIRWISE CONSTRAINT.

Class (Number of Pixels)	Producer’s Accuracy (%)					
	DPMM	Scaling+ DPMM	Proposed tDPMM	Scaling+ DPMM+MF	tDPMM+MF	Proposed tDPMM-PC
Woodland (35888)	59.72	33.00	88.68	35.92	94.80	93.76
Bare field (42280)	61.46	79.98	67.30	90.37	74.36	91.13
Crop 1 (5138)	78.18	22.47	72.74	18.19	80.76	98.44
Crop 2 (2730)	85.12	13.51	00.00	12.63	00.00	95.60
Roads (8841)	97.12	09.64	79.28	08.54	80.56	90.44
Buildings (11147)	18.85	40.01	59.62	44.62	60.92	56.93
OA (%)	60.78	49.51	73.26	54.81	78.78	88.84
κ	0.4983	0.3272	0.6399	0.3838	0.7087	0.8438

provides the metric values corresponding to the highest OA among 20 independent tests. For the other compared methods, we present the average values over 20 independent tests.

A. Effectiveness of the Introduced Texture Variable and the Pairwise Constraint in tDPMM-PC

In the proposed method (i.e., the variational tDPMM-PC), the texture variable and the pairwise constraint are incorporated. Their separate effects are investigated by performing classification based on the high-resolution PolSAR image ‘‘Oberp’’. In Fig. 2, we present the experimental results for the variational DPMM [see Appendix], our variational tDPMM [see Section III], and the proposed method [see Section IV]. The integrated method (i.e., the proposed tDPMM-PC) is also evaluated against the multi-step procedures of ‘‘Scaling+DPMM’’, ‘‘Scaling+DPMM+MF’’, and ‘‘tDPMM+MF’’. In the procedure of ‘‘Scaling+DPMM’’, the PolSAR data are first scaled according to $sC_n = C_n/t_n$, where $t_n = tr(\Omega^{-1} \cdot$

$C_n)/d$, Ω is the average of all observations in a PolSAR image, and d is the number of rows in the square matrix C_n . Subsequently, these scaled PolSAR data are classified by the variational DPMM method. The procedure of ‘‘Scaling+DPMM+MF’’ includes the scaling of data, the pixel-wise classification of the scaled data by the variational DPMM, and the post-processing by using the mode filter (MF) on the classification map. In the procedure of ‘‘tDPMM+MF’’, the pixel-wise classification by the variational tDPMM is performed and the MF is subsequently used as a post-processing step to remove noisy pixels in the classification map. The truncation level is set to the number of categories in the ground truth. The label for each pixel is determined according to (20). In this experiment, $W_{i0} = 1 \times 10^{-2} \cdot \mathbf{I}$ for all i . Here, \mathbf{I} is the identity matrix, where every entry in the diagonal is 1 and the other entries are 0.

According to Fig. 2(a) and (c), although the details in the black solid circle are recognized by the variational DPMM, it obviously misclassifies the building as the woodland in view of the result in the middle red circle. By incorporating the texture variable into the variational DPMM, the variational tDPMM is achieved. It is observed from Fig. 2(e) that the variational tDPMM correctly identifies the building (the yellow pixels) in the middle red circle. Moreover, the edges in the black dotted circle are well preserved by the variational tDPMM, and the better results for visual interpretation are observed in the woodland [see the red solid circle of Fig. 2(e)]. Compared with the multi-step procedure of ‘‘Scaling+DPMM’’ as shown in Fig. 2(d), the variational tDPMM clearly identifies the main structures. These improved results reveal that the incorporated texture variable in the variational tDPMM is beneficial to the analysis of PolSAR data both from high-resolution images and in heterogeneous areas.

By further exploiting the mode filter to reduce the noisy pixels in the classification maps, the ‘‘Scaling+DPMM+MF’’ and the ‘‘tDPMM+MF’’ significantly improve the overall accuracy (OA) values according to Table I. Nevertheless, their classification results still exhibit the ‘‘salt-and-pepper’’ appearance to some extent, and they suffer from the loss of details and the misclassification in the black solid circles of Fig. 2(f) and Fig. 2(g). By contrast, the proposed method significantly alleviates the ‘‘salt-and-pepper’’ effect and provides a classification map with less noisy points as shown in Fig. 2(h), implying the effectiveness of incorporating the local correlation through the pairwise constraint.

B. Low-Resolution PolSAR Images

According to the ground truth in Fig. 3(a), the PolSAR image ‘‘Kakadu’’ provides water body and natural areas, such as the mangroves, the woodland, and the grassland. The PolSAR image ‘‘San Francisco’’ includes a large part of urban area as shown in Fig. 4(a). With these two PolSAR images, we verify the effectiveness of the proposed method in identifying the natural areas as well as the urban area. The truncation level is set to the number of categories, which can be obtained from their ground-truth maps. In the experiment with data set ‘‘Kakadu’’, $W_{i0} = 1 \times 10^3 \cdot \mathbf{I}$ for all i ; in ‘‘San Francisco’’, $W_{i0} = 8 \times 10^1 \cdot \mathbf{I}$ for all i .

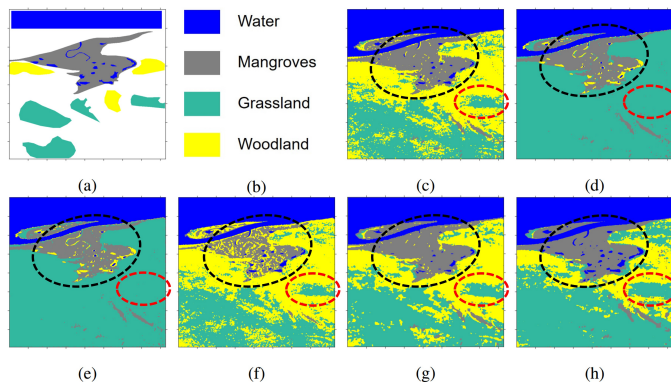


Fig. 3. Ground-truth map for data set “Kakadu” and classification maps obtained by the compared methods. (a) The ground truth. (b) The legend. (c) The H/α -Wishart-MRF method. (d) The Chernoff-Wishart-MRF method. (e) The variational DPMM-MRF method. (f) The variational tDPMM-MRF method. (g) The CV-CNN method. (h) The proposed method.

TABLE II
ACCURACY ASSESSMENT BASED ON DATA SET “KAKADU”.

Class (Number of Pixels)	Producer’s Accuracy (%)					
	Unsupervised H/α - Wishart-MRF	Unsupervised Chernoff- Wishart-MRF	Unsupervised Variational DPMM-MRF	Unsupervised Variational tDPMM-MRF	Supervised CV-CNN Method	Proposed Method
Water (81816)	95.26	92.43	92.61	95.70	93.89	98.37
Mangroves (76951)	90.23	88.04	85.97	64.43	94.03	93.62
Grassland (61327)	95.53	99.98	99.98	94.76	98.87	99.97
Woodland (28535)	99.72	00.00	00.00	94.94	99.74	89.91
OA (%)	94.28	82.33	81.74	85.70	95.82	96.32
κ	0.9215	0.7527	0.7448	0.8075	0.9424	0.9488

As shown in Fig. 3(d) and (e), the Chernoff-Wishart-MRF method and the variational DPMM-MRF method fail to discriminate the woodland from the grassland, leading to the misclassification and the loss of the details in the red circle. The other methods provide similar results to each other. However, according to Fig. 3(f), the variational tDPMM-MRF method tends to confuse the mangroves with the woodland pixels. Although the H/α -Wishart-MRF method and the CV-CNN method provide the structure information in the grassland and the woodland, they ignore the details in the mangrove area of the black dotted circle. The proposed method clearly identifies the water in the mangrove area and achieves the competitive classification performance with the CV-CNN method. The high accuracy values and the large κ in the last column of Table II confirm the effectiveness of the proposed method in identifying the natural areas.

In building areas and urban areas, houses, roads, cars, and trees could be mixed, leading to complicated scattering characteristics. As shown in the red circles of Fig. 4(c)-(e), there are many noisy points, and this urban area is not well identified by the three methods, i.e., the H/α -Wishart-MRF method, the Chernoff-Wishart-MRF method, and the variational DPMM-MRF method. All these three methods involve the complex Wishart distribution for either clustering or modeling PolSAR data. Thus, it is found that the complex Wishart distribution itself is not always adequate to accurately capture the heterogeneity in the urban area. According to Fig. 4(f) and (h), the variational tDPMM-MRF and the proposed method provide smooth results in the urban area [see the red

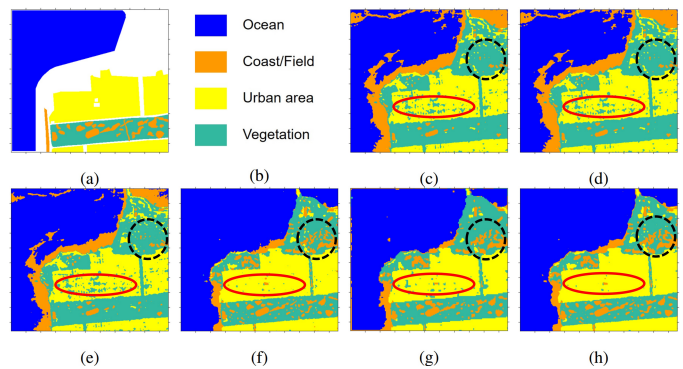


Fig. 4. Ground-truth map for data set “San Francisco” and classification maps obtained by the compared methods. (a) The ground truth. (b) The legend. (c) The H/α -Wishart-MRF method. (d) The Chernoff-Wishart-MRF method. (e) The variational DPMM-MRF method. (f) The variational tDPMM-MRF method. (g) The CV-CNN method. (h) The proposed method.

TABLE III
ACCURACY ASSESSMENT BASED ON DATA SET “SAN FRANCISCO”.

Class (Number of Pixels)	Producer’s Accuracy (%)					
	Unsupervised H/α - Wishart-MRF	Unsupervised Chernoff- Wishart-MRF	Unsupervised Variational DPMM-MRF	Unsupervised Variational tDPMM-MRF	Supervised CV-CNN Method	Proposed Method
Ocean (86567)	88.16	88.19	92.86	99.95	99.52	99.93
Coast/Field (8810)	33.00	33.00	35.48	66.90	72.84	72.11
Urban area (57735)	90.29	90.29	88.99	98.88	96.28	99.52
Vegetation (21834)	98.97	98.97	98.87	94.30	93.47	93.25
OA (%)	87.43	87.45	89.44	97.23	96.46	97.56
κ	0.8090	0.8092	0.8373	0.9558	0.9436	0.9611

circle] and better preserve the details in the black circles, which implies the effectiveness of the introduced texture variable in facilitating the analysis of the PolSAR data from the extremely heterogeneous areas. Moreover, the variational tDPMM-MRF and the proposed method achieve as good performance as the CV-CNN method according to Table III.

C. High-Resolution PolSAR Images

Data set “Foulum” is with the nominal range and azimuth pixel spacing (range \times azimuth in meter) of $1.49m \times 0.749m$. The resolution of data set “Oberp” is approximately $1.5m \times 1.5m$. With these two data sets, we can evaluate the performance of the proposed method for high-resolution PolSAR images. For data set “Foulum”, the proposed method adopts the parameter $W_{i0} = 1 \times 10^{-1} \cdot \mathbf{I}$ for all i ; for “Oberp”, $W_{i0} = 1 \times 10^{-2} \cdot \mathbf{I}$ for all i .

For data set “Foulum”, all the methods identify the main structures as shown in Fig. 5(c)-(h). However, they exhibit different patterns in the classification of the building areas (e.g., the area in the red dotted box). Specifically, the H/α -Wishart-MRF method, the Chernoff-Wishart-MRF method, the variational DPMM-MRF and the variational tDPMM-MRF method identify the building area as a combination of different categories in view of the staggered appearance of the orange and the yellow pixels in the red boxes, although all these methods have incorporated the local correlation. This staggered appearance leads to their low values in the accuracy of the building category according to Table IV. The CV-CNN method correctly recognizes the building area with less noisy

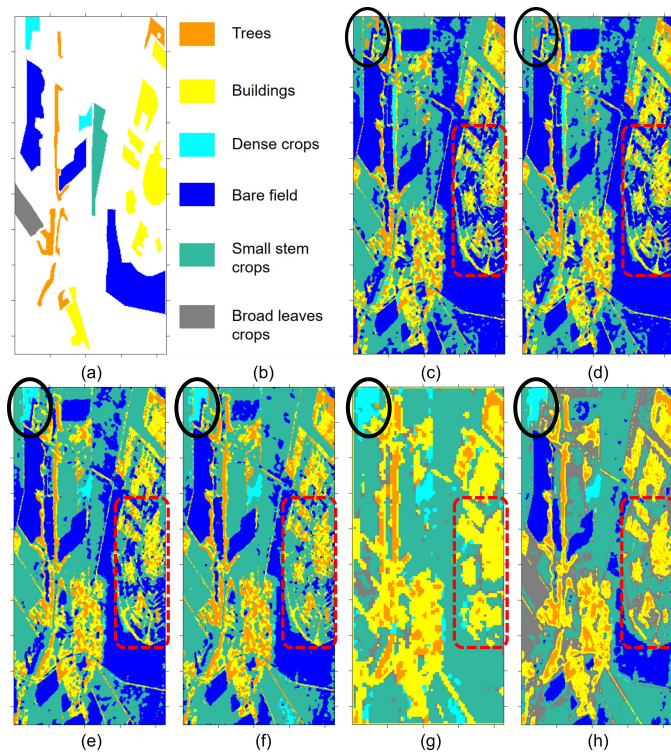


Fig. 5. Ground-truth map for data set “Foulum” and classification maps obtained by the compared methods. (a) The ground truth. (b) The legend. (c) The H/α -Wishart-MRF method. (d) The Chernoff-Wishart-MRF method. (e) The variational DPMM-MRF method. (f) The variational tDPMM-MRF method. (g) The CV-CNN method. (h) The proposed method.

TABLE IV
ACCURACY ASSESSMENT BASED ON DATA SET “FOULUM”.

Class (Number of Pixels)	Producer’s Accuracy (%)					
	Unsupervised		Unsupervised		Supervised	
	H/α - Wishart-MRF	Chernoff- Wishart-MRF	Variational DPMM-MRF	Variational tDPMM-MRF	CV-CNN Method	Proposed Method
Trees (3163)	54.75	55.26	67.24	83.15	73.67	68.33
Buildings (6734)	52.19	53.89	59.45	49.17	94.52	78.89
Dense crops (1005)	00.09	00.09	82.68	93.53	99.51	96.81
Bare field (9852)	99.43	99.44	99.13	96.75	00.00	85.51
Small stem crops (1971)	79.45	77.77	88.68	96.39	87.19	97.66
Broad leaves crops (1454)	00.00	00.00	00.00	00.00	47.40	98.62
OA (%)	68.69	69.10	76.41	75.74	45.84	83.67
κ	0.5751	0.5796	0.6791	0.6759	0.3649	0.7825

points, and it achieves the highest classification accuracy for the building category among the compared methods. However, it fails to distinguish the bare field from the small stem crops, which implies that the CV-CNN method requires more training samples for the bare field to achieve better discrimination. In Fig. 5(h), the proposed method tends to identify the building areas as the whole blocks and provides the convenience for the interpretation of the PoSAR data in the heterogeneous areas.

In data set “Oberp”, the H/α -Wishart-MRF method, the Chernoff-Wishart-MRF method, and the variational DPMM-MRF method bring about the complicated structures in the woodland according to the results in the red circles of the Fig. 6(c)-(e). Although they preserve the main structures of the woodland, the results are not convenient for visual interpretation. By contrast, in Fig. 6(f) and (h), the variational tDPMM-MRF and the proposed method demonstrate less

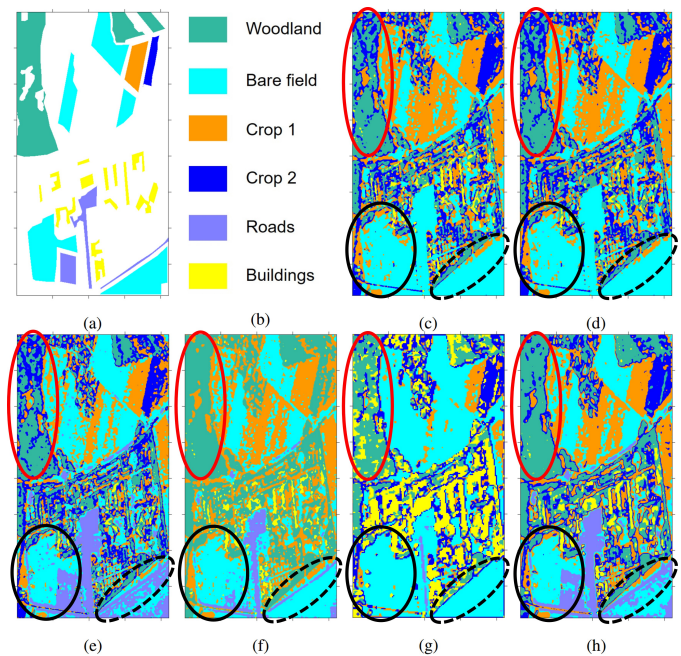


Fig. 6. Ground-truth map for data set “Oberp” and classification maps obtained by the compared methods. (a) The ground truth. (b) The legend. (c) The H/α -Wishart-MRF method. (d) The Chernoff-Wishart-MRF method. (e) The variational DPMM-MRF method. (f) The variational tDPMM-MRF method. (g) The CV-CNN method. (h) The proposed method.

TABLE V
ACCURACY ASSESSMENT BASED ON DATA SET “OBERP”.

Class (Number of Pixels)	Producer’s Accuracy (%)					
	Unsupervised		Unsupervised		Supervised	
	H/α - Wishart-MRF	Chernoff- Wishart-MRF	Variational DPMM-MRF	Variational tDPMM-MRF	CV-CNN Method	Proposed Method
Woodland (35888)	75.52	67.52	65.20	98.53	69.83	93.76
Bare field (42280)	91.41	92.12	83.16	95.77	98.65	91.13
Crop 1 (5138)	97.85	98.32	92.81	97.39	74.13	98.44
Crop 2 (2730)	99.04	99.41	95.78	00.00	85.44	95.60
Roads (8841)	00.00	00.00	94.43	65.05	16.34	90.44
Buildings (11147)	38.94	17.85	17.34	45.07	93.42	56.93
OA (%)	73.40	68.79	71.89	86.43	80.28	88.84
κ	0.6259	0.5620	0.6249	0.8016	0.7167	0.8438

noisy points in the heterogeneous area (i.e., the woodland in the red circle) and can still preserve the main structures (e.g., the two regions with orange pixels in the red circle), revealing that both the introduced texture variable and the incorporation of local correlation are beneficial to the visual interpretation of the heterogeneous area. In particular, the variational tDPMM-MRF better preserves the structure in the black dotted circle of Fig. 6(f). In this experiment, the CV-CNN method also provides the accurate classification of the buildings in view of both its classification map in Fig. 6(g) and its high accuracy of the building category in Table V. Nevertheless, the proposed method identifies the structures in the black solid circle as shown in Fig. 6(h), providing a more appropriate classification map.

D. Classification of Agriculture Area

The crop classification is performed based on data set “Flevoland”. Its ground truth [36] and legend are presented in Fig. 7(a) and (b). According to the ground truth, 8 types

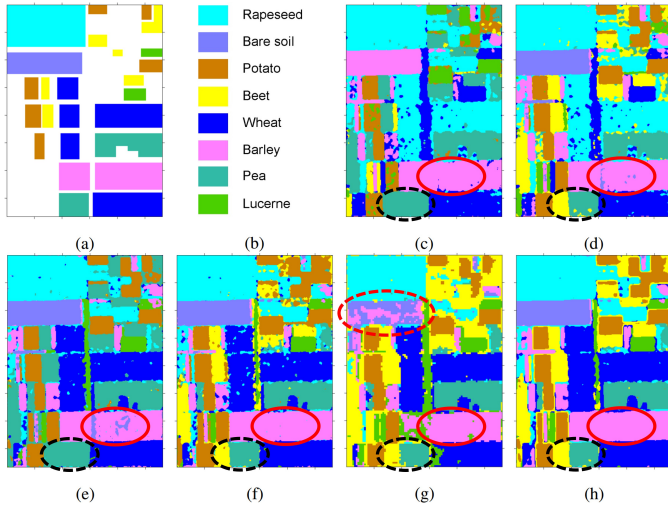


Fig. 7. Ground-truth map for data set “Flevoland” and classification maps obtained by the compared methods. (a) The ground truth. (b) The legend. (c) The H/α -Wishart-MRF method. (d) The Chernoff-Wishart-MRF method. (e) The variational DPMM-MRF method. (f) The variational tDPMM-MRF method. (g) The CV-CNN method. (h) The proposed method.

TABLE VI
ACCURACY ASSESSMENT BASED ON DATA SET “FLEVOLAND”.

Class (Number of Pixels)	Producer’s Accuracy (%)					
	Unsupervised		Unsupervised		Supervised	
	H/α - Wishart-MRF	Chernoff- Wishart-MRF	Variational DPMM-MRF	Variational tDPMM-MRF	CV-CNN Method	Proposed Method
Rapeseed (11011)	98.58	98.50	97.62	99.08	96.14	99.43
Bare soil (5343)	00.00	97.26	97.54	96.96	60.62	97.62
Potato (5123)	60.97	99.33	98.49	99.62	96.59	98.24
Beet (4308)	04.36	80.75	00.06	67.82	97.32	83.02
Wheat (15208)	37.29	38.06	98.29	97.56	95.09	99.56
Barley (8729)	97.96	98.82	94.27	99.17	79.61	99.01
Peas(6842)	98.12	96.40	98.20	97.89	96.30	97.54
Lucerne (1450)	00.00	00.00	82.20	96.68	97.07	92.92
OA (%)	60.50	78.63	89.80	96.03	90.33	97.52
κ	0.5277	0.7466	0.8777	0.9525	0.8838	0.9704

of crops are provided for quantitative evaluation. In this experiment, $W_{i0} = 3 \times 10^{-1} \cdot \mathbf{I}$ is set for the proposed method.

In agriculture areas, the same type of crops can be always found in a local region. Thus, it is generally valid to assume the existence of the local correlation for the classification of agriculture areas. Smoothing results can be found from Fig. 7(c)-(h), implying the effectiveness of both the MRF and the pairwise constraint. In Fig. 7(d) and (e), the Chernoff-Wishart-MRF method and the variational DPMM-MRF method do not provide the coinciding results with the ground truth in view of the structures in the red circles. By contrast, the proposed method identifies the whole block of Barley and correctly separates the region in the lower black circle into two parts as shown in Fig. 7(h). By a comparison between Fig. 7(f) and (h), the variational tDPMM-MRF exhibits the competitive performance with the proposed method, which is also confirmed by the high producer’s accuracy in Table VI. Nevertheless, the proposed method achieves both the higher OA and the higher κ , implying the good classification performance of the proposed method in the agriculture area.

VI. CONCLUSION

A textured Dirichlet process mixture model with the pairwise constraint (tDPMM-PC) has been proposed for unsupervised classification of PolSAR images. The proposed model integrated the texture variable into the DPMM to provide more flexibility in characterizing the PolSAR data in the heterogeneous and the extremely heterogeneous areas. Furthermore, the similarity measure has been presented to quantitatively describe the relation between paired pixels. Thus, local correlation can be conveniently taken into account through the pairwise constraint, producing appropriate results for visual interpretation. The variational learning algorithm for the proposed model (i.e., tDPMM-PC) was developed with all the closed-form updates. The effectiveness of the proposed method has been verified with the low-resolution PolSAR images and the high-resolution PolSAR images, which provide the homogeneous areas, the heterogeneous areas, and the extremely heterogeneous areas.

In the proposed method, the local correlation (i.e., the contextual information in the neighborhood) has been incorporated to provide better results for visual interpretation. However, the edge information was not well preserved. We will further consider the edge information for PolSAR image classification so as to clearly and accurately preserve boundaries. In addition, more experiments are needed to investigate the different effects of the pairwise constraint and the MRF for low-resolution and high-resolution PolSAR images.

APPENDIX VARIATIONAL DPMM

In the Dirichlet process mixture of the complex Wishart distributions, data are generated according to the complex Wishart distribution. Following the principle of the variational inference, the update equations for this Dirichlet process mixture model (DPMM) are derived as

$$\beta_i = 1 + \sum_n \mathbf{E}[z_{ni}], \quad (50a)$$

$$\alpha_i = \alpha_0 + \sum_{j=i+1}^{\infty} \sum_n \mathbf{E}[z_{nj}], \quad (50b)$$

$$\eta_i = \eta_{i0} + L \sum_n \mathbf{E}[z_{ni}], \quad (50c)$$

$$W_i = \frac{1}{\eta_i} \left\{ \eta_{i0} W_{i0} + L \sum_n \mathbf{E}[z_{ni}] C_n \right\}, \quad (50d)$$

$$\mathbf{E}[z_{ni}] = \frac{\rho_{ni}}{\sum_i \rho_{ni}}. \quad (50e)$$

The logarithm of ρ_{ni} is given by

$$\begin{aligned} \ln \rho_{ni} = & \mathbf{E}[\ln \omega_i(\mathbf{v})] + \ln \frac{L^L d}{\Gamma_d(L)} + L \mathbf{E}[\ln |\Omega_i|] \\ & + (L - d) \ln |C_n| - L \cdot \text{tr} \left(\mathbf{E}[\Omega_i] \cdot C_n \right), \end{aligned} \quad (51)$$

where $\mathbf{E}[\ln \omega_i(\mathbf{v})] = \mathbf{E}[\ln v_i] + \sum_{j=1}^{i-1} \mathbf{E}[\ln(1 - v_j)]$, and $\text{tr}(\cdot)$ is the trace operator. The involved expectation values can be evaluated based on (37). Thus, the DPMM can be learned by alternatively implementing (50a)-(50e), until the

stop criterion is reached. Furthermore, according to (20), the labels for PolSAR data can be determined.

ACKNOWLEDGMENT

The authors would like to thank European Space Agency (ESA) and Jet Propulsion Laboratory (JPL) for providing the PolSAR images. The authors would also like to thank the editors and the anonymous reviewers for their careful reading and valuable comments, which are greatly helpful in improving the quality of this paper. Wenzhi Liao is a post-doctoral fellow of the Research Foundation Flanders (FWO-Vlaanderen, Belgium) and acknowledges its support.

REFERENCES

[1] K. Sirinukunwattana, S. E. A. Raza, Y. W. Tsang, D. R. J. Snead, I. A. Cree, and N. M. Rajpoot, "Locality sensitive deep learning for detection and classification of nuclei in routine colon cancer histology images," *IEEE Trans. Med. Imag.*, vol. 35, no. 5, pp. 1196–1206, May 2016.

[2] S. Manivannan, C. Cobb, S. Burgess, and E. Trucco, "Subcategory classifiers for multiple-instance learning and its application to retinal nerve fiber layer visibility classification," *IEEE Trans. Med. Imag.*, vol. 36, no. 5, pp. 1140–1150, May 2017.

[3] K. Kayabol and J. Zerubia, "Unsupervised amplitude and texture classification of SAR images with multinomial latent model," *IEEE Trans. Image Process.*, vol. 22, no. 2, pp. 561–572, Feb. 2013.

[4] H. Lee and H. Kwon, "Going deeper with contextual CNN for hyperspectral image classification," *IEEE Trans. Image Process.*, vol. 26, no. 10, pp. 4843–4855, Oct. 2017.

[5] W. Wu, H. Guo, and X. Li, "Urban area SAR image man-made target extraction based on the product model and the time-frequency analysis," *IEEE J. Sel. Topics Appl. Earth Observ. Remote Sens.*, vol. 8, no. 3, pp. 943–952, Mar. 2015.

[6] J. Wei, P. Li, J. Yang, J. Zhang, and F. Lang, "A new automatic ship detection method using L-band polarimetric SAR imagery," *IEEE J. Sel. Topics Appl. Earth Observ. Remote Sens.*, vol. 7, no. 4, pp. 1383–1393, Apr. 2014.

[7] V. Akbari, A. P. Doulgeris, and T. Eltoft, "Monitoring glacier changes using multitemporal multipolarization SAR images," *IEEE Trans. Geosci. Remote Sens.*, vol. 52, no. 6, pp. 3729–3741, Jun. 2014.

[8] X. Li, H. Guo, L. Zhang, X. Chen, and L. Liang, "A new approach to collapsed building extraction using RADARSAT-2 polarimetric SAR imagery," *IEEE Geosci. Remote Sens. Lett.*, vol. 9, no. 4, pp. 677–681, Jul. 2012.

[9] J.-S. Lee, M. R. Grunes, T. L. Ainsworth, L. J. Du, D. L. Schuler, and S. R. Cloude, "Unsupervised classification using polarimetric decomposition and the complex Wishart classifier," *IEEE Trans. Geosci. Remote Sens.*, vol. 37, no. 5, pp. 2249–2258, Sep. 1999.

[10] S. R. Cloude and E. Pottier, "An entropy based classification scheme for land applications of polarimetric SAR," *IEEE Trans. Geosci. Remote Sens.*, vol. 35, no. 1, pp. 68–78, Jan. 1997.

[11] J.-S. Lee, M. R. Grunes, and R. Kwok, "Classification of multi-look polarimetric SAR imagery based on complex Wishart distribution," *Int. J. Remote Sens.*, vol. 15, no. 11, pp. 2299–2311, 1994.

[12] F. Cao, W. Hong, Y. Wu, and E. Pottier, "An unsupervised segmentation with an adaptive number of clusters using the SPAN/H α /A space and the complex Wishart clustering for fully polarimetric SAR data analysis," *IEEE Trans. Geosci. Remote Sens.*, vol. 45, no. 11, pp. 3454–3467, Nov. 2007.

[13] E. Pottier, "The H/A/ α polarimetric decomposition approach applied to PolSAR data processing," in *Proc. PIERS Workshop Adv. Radar Methods*, Baveno, Italy, Jul. 1998, pp. 120–122.

[14] S. Wang, K. Liu, J. Pei, M. Gong, and Y. Liu, "Unsupervised classification of fully polarimetric SAR images based on scattering power entropy and copolarized ratio," *IEEE Geosci. Remote Sens. Lett.*, vol. 10, no. 3, pp. 622–626, May 2013.

[15] C. J. Oliver and S. Quegan, *Understanding synthetic aperture radar images*. Raleigh, NC: SciTech Publishing, 2004.

[16] J.-S. Lee and E. Pottier, *Polarimetric Imaging: From Basics to Applications*. Boca Raton, FL: CRC Press, 2009.

[17] N. R. Goodman, "Statistical analysis based on a certain multivariate complex Gaussian distribution (an introduction)," *Ann. Math. Statist.*, vol. 34, no. 1, pp. 152–177, Mar. 1963.

[18] P. R. Kersten, J.-S. Lee, and T. L. Ainsworth, "Unsupervised classification of polarimetric synthetic aperture radar images using fuzzy clustering and EM clustering," *IEEE Trans. Geosci. Remote Sens.*, vol. 43, no. 3, pp. 519–527, Mar. 2005.

[19] M. Dabboor, M. J. Collins, V. Karathanassi, and A. Braun, "An unsupervised classification approach for polarimetric SAR data based on the Chernoff distance for complex Wishart distribution," *IEEE Trans. Geosci. Remote Sens.*, vol. 51, no. 7, pp. 4200–4213, Jul. 2013.

[20] L. Du and J.-S. Lee, "Fuzzy classification of earth terrain covers using multi-look polarimetric SAR image data," *Int. J. Remote Sens.*, vol. 17, no. 4, pp. 809–826, 1996.

[21] W. Wang, D. Xiang, J. Zhang, and J. Wan, "Integrating contextual information with H/ α decomposition for PolSAR data classification," *IEEE Geosci. Remote Sens. Lett.*, vol. 13, no. 12, pp. 2034–2038, Dec. 2016.

[22] X. Deng, C. López-Martínez, J. S. Chen, and P. P. Han, "Statistical modeling of polarimetric SAR data: A survey and challenges," *Remote Sensing*, vol. 9, no. 4, p. 348, 2017.

[23] X. Deng and C. López-Martínez, "Analysis of texture distributions of polarimetric SAR data," in *2015 IEEE International Geoscience and Remote Sensing Symposium (IGARSS)*, Jul. 2015, pp. 3802–3805.

[24] X. Deng, C. López-Martínez, and E. M. Varona, "A physical analysis of polarimetric SAR data statistical models," *IEEE Trans. Geosci. Remote Sens.*, vol. 54, no. 5, pp. 3035–3048, May 2016.

[25] M. S. Greco and F. Gini, "Statistical analysis of high-resolution SAR ground clutter data," *IEEE Trans. Geosci. Remote Sens.*, vol. 45, no. 3, pp. 566–575, Mar. 2007.

[26] I. R. Joughin, D. P. Winebrenner, and D. B. Percival, "Probability density functions for multilook polarimetric signatures," *IEEE Trans. Geosci. Remote Sens.*, vol. 32, no. 3, pp. 562–574, May 1994.

[27] A. Lopès and F. Séry, "Optimal speckle reduction for the product model in multilook polarimetric SAR imagery and the Wishart distribution," *IEEE Trans. Geosci. Remote Sens.*, vol. 35, no. 3, pp. 632–647, May 1997.

[28] J.-S. Lee, D. L. Schuler, R. H. Lang, and K. J. Ranson, "K-distribution for multi-look processed polarimetric SAR imagery," in *Proc. IEEE IGARSS*, vol. 4, Pasadena, CA, 1994, pp. 2179–2181.

[29] C. C. Freitas, A. C. Frery, and A. H. Correia, "The polarimetric \mathcal{G} distribution for SAR data analysis," *Environmetrics*, vol. 16, no. 1, pp. 13–31, Feb. 2005.

[30] S. Khan and R. Guida, "Application of Mellin-kind statistics to polarimetric \mathcal{G} distribution for SAR data," *IEEE Trans. Geosci. Remote Sens.*, vol. 52, no. 6, pp. 3513–3528, Jun. 2014.

[31] L. Bombrun and J.-M. Beaulieu, "Fisher distribution for texture modeling of polarimetric SAR data," *IEEE Geosci. Remote Sens. Lett.*, vol. 5, no. 3, pp. 512–516, Jul. 2008.

[32] W. Song, M. Li, P. Zhang, Y. Wu, L. Jia, and L. An, "The W \mathcal{G} distribution for multilook polarimetric SAR data and its application," *IEEE Geosci. Remote Sens. Lett.*, vol. 12, no. 10, pp. 2056–2060, Oct. 2015.

[33] C. Liu, H.-C. Li, X. Sun, and W. J. Emery, "H distribution for multilook polarimetric SAR data," *IEEE Geosci. Remote Sens. Lett.*, vol. 14, no. 4, pp. 489–493, Apr. 2017.

[34] A. P. Doulgeris, S. N. Anfinsen, and T. Eltoft, "Automated non-Gaussian clustering of polarimetric synthetic aperture radar images," *IEEE Trans. Geosci. Remote Sens.*, vol. 49, no. 10, pp. 3665–3676, Oct. 2011.

[35] J. I. Fernández-Michelli, M. Hurtado, J. A. Areta, and C. H. Muravchik, "Unsupervised polarimetric SAR image classification using \mathcal{G}_p^0 mixture model," *IEEE Geosci. Remote Sens. Lett.*, vol. 14, no. 5, pp. 754–758, May 2017.

[36] Y. H. Wu, K. Ji, W. Yu, and Y. Su, "Region-based classification of polarimetric SAR images using Wishart MRF," *IEEE Geosci. Remote Sens. Lett.*, vol. 5, no. 4, pp. 668–672, Oct. 2008.

[37] B. Liu, H. Hu, H. Wang, K. Wang, X. Liu, and W. Yu, "Superpixel-based classification with an adaptive number of classes for polarimetric SAR images," *IEEE Trans. Geosci. Remote Sens.*, vol. 51, no. 2, pp. 907–924, Feb. 2013.

[38] M. Schroder, H. Rehrauer, K. Seidel, and M. Datcu, "Spatial information retrieval from remote-sensing images. II. Gibbs-Markov random fields," *IEEE Trans. Geosci. Remote Sens.*, vol. 36, no. 5, pp. 1446–1455, Sep. 1998.

[39] E. Rignot and R. Chellappa, "Segmentation of polarimetric synthetic aperture radar data," *IEEE Trans. Image Process.*, vol. 1, no. 3, pp. 281–300, Jul. 1992.

[40] L. Denis, F. Tupin, J. Darbon, and M. Sigelle, "SAR image regularization with fast approximate discrete minimization," *IEEE Trans. Image Process.*, vol. 18, no. 7, pp. 1588–1600, Jul. 2009.

- [41] C. A. Deledalle, L. Denis, and F. Tupin, "Iterative weighted maximum likelihood denoising with probabilistic patch-based weights," *IEEE Trans. Image Process.*, vol. 18, no. 12, pp. 2661–2672, Dec. 2009.
- [42] X. Yang, X. Gao, D. Tao, X. Li, and J. Li, "An efficient MRF embedded level set method for image segmentation," *IEEE Trans. Image Process.*, vol. 24, no. 1, pp. 9–21, Jan. 2015.
- [43] A. P. Doulgeris, "An automatic U -distribution and Markov random field segmentation algorithm for PolSAR images," *IEEE Trans. Geosci. Remote Sens.*, vol. 53, no. 4, pp. 1819–1827, Apr. 2015.
- [44] X. Yang, X. Gao, B. Song, N. Wang, and D. Yang, "ASI aurora search: an attempt of intelligent image processing for circular fisheye lens," *Opt. Express*, vol. 26, no. 7, pp. 7985–8000, Apr. 2018.
- [45] X. Cao, F. Zhou, L. Xu, D. Meng, Z. Xu, and J. Paisley, "Hyperspectral image classification with Markov random fields and a convolutional neural network," *IEEE Trans. Image Process.*, vol. 27, no. 5, pp. 2354–2367, May 2018.
- [46] J. Lafferty, A. McCallum, and F. Pereira, "Conditional random fields: Probabilistic models for segmenting and labeling sequence data," in *Proc. 18th International Conf. on Machine Learning*, 2001, pp. 282–289.
- [47] G. Zhang and X. Jia, "Simplified conditional random fields with class boundary constraint for spectral-spatial based remote sensing image classification," *IEEE Geosci. Remote Sens. Lett.*, vol. 9, no. 5, pp. 856–860, Sep. 2012.
- [48] Y. Zhong, X. Lin, and L. Zhang, "A support vector conditional random fields classifier with a Mahalanobis distance boundary constraint for high spatial resolution remote sensing imagery," *IEEE J. Sel. Topics Appl. Earth Observ. Remote Sens.*, vol. 7, no. 4, pp. 1314–1330, Apr. 2014.
- [49] P. Zhang, M. Li, Y. Wu, and H. Li, "Hierarchical conditional random fields model for semisupervised SAR image segmentation," *IEEE Trans. Geosci. Remote Sens.*, vol. 53, no. 9, pp. 4933–4951, Sep. 2015.
- [50] F. Wang, Y. Wu, M. Li, P. Zhang, and Q. Zhang, "Adaptive hybrid conditional random field model for SAR image segmentation," *IEEE Trans. Geosci. Remote Sens.*, vol. 55, no. 1, pp. 537–550, Jan. 2017.
- [51] X. Su, C. He, Q. Feng, X. Deng, and H. Sun, "A supervised classification method based on conditional random fields with multiscale region connection calculus model for SAR image," *IEEE Geosci. Remote Sens. Lett.*, vol. 8, no. 3, pp. 497–501, May 2011.
- [52] J. Zhao, Y. Zhong, H. Shu, and L. Zhang, "High-resolution image classification integrating spectral-spatial-location cues by conditional random fields," *IEEE Trans. Image Process.*, vol. 25, no. 9, pp. 4033–4045, Sep. 2016.
- [53] K. Wagstaff, C. Cardie, S. Rogers, and S. Schrödl, "Constrained k -means clustering with background knowledge," in *ICML*, vol. 1, 2001, pp. 577–584.
- [54] R. He, M. Zhang, L. Wang, Y. Ji, and Q. Yin, "Cross-modal subspace learning via pairwise constraints," *IEEE Trans. Image Process.*, vol. 24, no. 12, pp. 5543–5556, Dec. 2015.
- [55] X. Cao, C. Zhang, C. Zhou, H. Fu, and H. Foroosh, "Constrained multi-view video face clustering," *IEEE Trans. Image Process.*, vol. 24, no. 11, pp. 4381–4393, Nov. 2015.
- [56] J. Chen, Z. Zhang, and Y. Wang, "Relevance metric learning for person re-identification by exploiting listwise similarities," *IEEE Trans. Image Process.*, vol. 24, no. 12, pp. 4741–4755, Dec. 2015.
- [57] H. Bi, J. Sun, and Z. Xu, "A graph-based semisupervised deep learning model for PolSAR image classification," *IEEE Transactions on Geoscience and Remote Sensing*, pp. 1–17, 2018.
- [58] H. Liu, Z. Wang, F. Shang, S. Yang, S. Gou, and L. Jiao, "Semi-supervised tensorial locally linear embedding for feature extraction using PolSAR data," *IEEE J. Sel. Topics Signal Process.*, vol. 12, no. 6, pp. 1476–1490, Dec. 2018.
- [59] T. S. Ferguson, "A Bayesian analysis of some nonparametric problems," *The Annals of Statistics*, pp. 209–230, 1973.
- [60] C. E. Antoniak, "Mixtures of Dirichlet processes with applications to Bayesian nonparametric problems," *The Annals of Statistics*, vol. 2, no. 6, pp. 1152–1174, 1974.
- [61] D. M. Blei and M. I. Jordan, "Variational inference for Dirichlet process mixtures," *Bayesian Analysis*, vol. 1, no. 1, pp. 121–143, 2006.
- [62] C. M. Bishop, *Pattern Recognition and Machine Learning*. New York: Springer-Verlag, 2006.
- [63] R. M. Neal, "Markov chain sampling methods for Dirichlet process mixture models," *Journal of Computational and Graphical Statistics*, vol. 9, no. 2, pp. 249–265, 2000.
- [64] Y. W. Teh, "Dirichlet process," in *Encyclopedia of machine learning*. Springer, 2011, pp. 280–287.
- [65] J. Sethuraman, "A constructive definition of Dirichlet priors," *Statistica Sinica*, vol. 4, no. 2, pp. 639–650, 1994.
- [66] S. Cui, G. Schwarz, and M. Datcu, "A comparative study of statistical models for multilook SAR images," *IEEE Geosci. Remote Sens. Lett.*, vol. 11, no. 10, pp. 1752–1756, Oct. 2014.
- [67] P. Shaman, "The inverted complex Wishart distribution and its application to spectral estimation," *Journal of Multivariate Analysis*, vol. 10, no. 1, pp. 51–59, 1980.
- [68] F. Forbes and N. Peyrard, "Hidden Markov random field model selection criteria based on mean field-like approximations," *IEEE Trans. Pattern Anal. Mach. Intell.*, vol. 25, no. 9, pp. 1089–1101, Sep. 2003.
- [69] S. P. Chatzis and G. Tsechpenakis, "The infinite hidden Markov random field model," *IEEE Trans. Neural Netw.*, vol. 21, no. 6, pp. 1004–1014, June 2010.
- [70] D. G. Tzikas, A. C. Likas, and N. P. Galatsanos, "The variational approximation for Bayesian inference," *IEEE Signal Process. Mag.*, vol. 25, no. 6, pp. 131–146, Nov. 2008.
- [71] R. Yan, J. Zhang, J. Yang, and A. G. Hauptmann, "A discriminative learning framework with pairwise constraints for video object classification," *IEEE Trans. Pattern Anal. Mach. Intell.*, vol. 28, no. 4, pp. 578–593, Apr. 2006.
- [72] J. Yu, D. Liu, D. Tao, and H. S. Seah, "Complex object correspondence construction in two-dimensional animation," *IEEE Trans. Image Process.*, vol. 20, no. 11, pp. 3257–3269, Nov. 2011.
- [73] Z. Lu and T. K. Leen, "Semi-supervised clustering with pairwise constraints: A discriminative approach," in *Artificial Intelligence and Statistics*, 2007, pp. 299–306.
- [74] J. Paisley, C. Wang, D. M. Blei, and M. I. Jordan, "Nested hierarchical Dirichlet processes," *IEEE Trans. Pattern Anal. Mach. Intell.*, vol. 37, no. 2, pp. 256–270, Feb. 2015.
- [75] J.-S. Lee, M. R. Grunes, and G. de Grandi, "Polarimetric SAR speckle filtering and its implication for classification," *IEEE Trans. Geosci. Remote Sens.*, vol. 37, no. 5, pp. 2363–2373, Sep. 1999.
- [76] Z. Zhang, H. Wang, F. Xu, and Y. Q. Jin, "Complex-valued convolutional neural network and its application in polarimetric SAR image classification," *IEEE Trans. Geosci. Remote Sens.*, vol. 55, no. 12, pp. 7177–7188, Dec. 2017.



Chi Liu received the B.Sc. degree and M.Sc. degree from Southwest Jiaotong University, Chengdu, China, in 2009 and 2012. He is currently working towards to the Ph.D. degree in signal and information processing in School of Information Science and Technology, Southwest Jiaotong University, China, and the Ph.D. degree in Computer Science Engineering from Ghent University, Belgium. His research interests include machine learning, image classification, and remote sensing image processing and analysis.



Heng-Chao Li (S'06–M'08–SM'14) received the B.Sc. and M.Sc. degrees from Southwest Jiaotong University, Chengdu, China, in 2001 and 2004, respectively, and the Ph.D. degree from the Graduate University of Chinese Academy of Sciences, Beijing, China, in 2008, all in information and communication engineering.

From 2013 to 2014, he was a Visiting Scholar with Prof. W. J. Emery at the University of Colorado at Boulder, Boulder, CO, USA. He is currently a Professor with the Sichuan Provincial Key Laboratory of Information Coding and Transmission, Southwest Jiaotong University, Chengdu. His research interests include the statistical analysis of synthetic aperture radar images, remote sensing image processing, and signal processing in communications.

Dr. Li received several scholarships or awards, especially including the Special Grade of the Financial Support from China Postdoctoral Science Foundation in 2009 and the New Century Excellent Talents in University from the Ministry of Education of China in 2011. He has also been a Reviewer for several international journals and conferences, such as the IEEE TRANSACTIONS ON GEOSCIENCE AND REMOTE SENSING, the IEEE JOURNAL OF SELECTED TOPICS IN APPLIED EARTH OBSERVATIONS AND REMOTE SENSING, the IEEE GEOSCIENCE AND REMOTE SENSING LETTERS, the IEEE TRANSACTIONS ON IMAGE PROCESSING, *IET Radar, Sonar and Navigation*, and the *Canadian Journal of Remote Sensing*. He is currently serving as an Associate Editor of the IEEE JOURNAL OF SELECTED TOPICS IN APPLIED EARTH OBSERVATIONS AND REMOTE SENSING.



Wenzhi Liao (S'10–M'14–SM'16) received the B.Sc. degree in mathematics from Hainan Normal University, Haikou, China, in 2006, the Ph.D. degree in engineering from South China University of Technology, Guangzhou, China, in 2012, and the Ph.D. degree in computer science engineering from Ghent University, Ghent, Belgium, in 2012.

Since 2012, he has been working first as a Postdoc at Ghent University and then as a Postdoctoral Research Fellow for the Research Foundation Flanders (FWO-Vlaanderen, Belgium). His current research

interests include pattern recognition, remote sensing, and image processing. In particular, his interests include mathematical morphology, multitask feature learning, multisensor data fusion, and hyperspectral image restoration.

Dr. Liao is a Senior Member of the IEEE, and serving as an Associate Editor for the IET IMAGE PROCESSING. He received the Best Paper Challenge Awards on both 2013 IEEE GRSS Data Fusion Contest and 2014 IEEE GRSS Data Fusion Contest.



Wilfried Philips (S'90–M'93–SM'10) was born in Aalst, Belgium, on October 19, 1966. He received the Diploma degree in electrical engineering and the Ph.D. degree in applied sciences, both from Ghent University, Ghent, Belgium, in 1989 and 1993, respectively.

Since November 1997, he has been a Lecturer in the Department of Telecommunications and Information Processing, Ghent University. He is currently a Senior Full Professor in the Department of Telecommunications and Information Processing,

Ghent University, where he heads the research group "Image Processing and Interpretation". His main research interests include the domains of image and video restoration and analysis.



William J. Emery (M'90–SM'01–F'02) received the Ph.D. degree in physical oceanography from the University of Hawaii, Honolulu, HI, USA, in 1975.

He was with Texas A&M University, College Station, TX, USA. In 1978, he joined the University of British Columbia, Vancouver, BC, Canada, where he was involved in Satellite Oceanography Facility/Education/Research Program. In 1987, he was a Professor of aerospace engineering sciences with the University of Colorado, Boulder, CO, USA.

He is currently an Adjunct Professor of informatics with Tor Vergata University, Rome, Italy. He has authored over 182 refereed publications, two textbooks, and over 150 conference papers.

Dr. Emery was an Elected Fellow of the American Meteorological Society in 2010, the American Astronautical Society in 2011, and the American Geophysical Union in 2012. He was a recipient of the 2004 IEEE Geoscience and Remote Sensing Society (GRSS) Educational Award and the 2009 GRSS Outstanding Service Award. He was the Chair of the IEEE Periodicals Committee that oversees the publication of 171 journals. He is the Vice President of Publications of the IEEE GRSS. He was the Founding Editor of the IEEE GEOSCIENCE AND REMOTE SENSING LETTERS in 2004 and the Editor-in-Chief of the IEEE GEOSCIENCE AND REMOTE SENSING LETTERS for six years. He serves as the Editor-in-Chief for the *Journal of the American Mathematical Society*.